Localised corrosion attacks and oxide growth on copper in phosphate-buffered saline

Jiaqi Luo, Christina Hein, Jean-François Pierson, Frank Mücklich

Version of Record: https://www.sciencedirect.com/science/article/pii/S1044580319321291
Manuscript_3f681f60e2209ad7ae906dc843229164

Localised corrosion attacks and oxide growth on copper in phosphate-buffered saline

Jiaqi Luo[a,b,*], Christina Hein[c], Jean-François Pierson[b], Frank Mücklich[a]

[a] Functional Materials, Saarland University, 66123 Saarbruecken, Germany

[b] Université de Lorraine, CNRS, IJL, F-54000 Nancy, France

[c] Inorganic Solid State Chemistry, Saarland University, 66123 Saarbruecken, Germany

[*] Email address: jiaqi.luo@uni-saarland.de

Abstract

Phosphate-buffered saline (PBS) is a buffer commonly used in antibacterial surface research. However, how copper surface varies in the buffer, in terms of corrosion attack and oxide growth, is not yet fully recognised. In this study, PBS was applied as droplet on two types of copper surface: ground and electropolished. By scanning electron microscope (SEM), the similarities of their corrosion sites were compared, revealing the initiation of intergranular attack and orientation-dependent crystallographic etching. High resolution grazing incidence X-ray diffractometer (GIXRD), optical microscope (OM), Raman spectroscopy and electron backscatter diffraction (EBSD) together provided detailed description of the epitaxial growth of cuprous oxide (Cu_2O) on electropolished copper. The amount of copper ion released from two types of surface were determined by inductively coupled plasma mass spectrometry (ICP-MS). The inhibition of Cu_2O growth on electropolished coupon by introducing *E. coli* into PBS was observed. However, bacteria were found to hardly alter the corrosion mechanisms or the distribution of corrosion sites.

Keywords: copper, cuprous oxide, PBS, intergranular corrosion, orientation, *E. coli*

1. Introduction

Copper and its alloys have been regarded as important candidates in microbiology or hygiene market [1]. This should be credited to their capability to release copper ions, which have been proved to exhibit strong antimicrobial effect [2, 3]. Therefore studies have been performed in order to understand from the phenomena such as cell damage and the mechanism of copper-DNA binding [4]. Tasks belong to materials researchers, on the other hand, are to figure out the approaches to incorporate copper into/onto different materials/surfaces [5-7], according to each of their application field [8-10]. Take the clinical environment as an example, touch surfaces made of coppers are promising in coping with not only those common germs such as *E. coli* or *S. aureus* [11-13], but also those deadly pathogenic strains/microbes such as *E. coli* O157 [14] and Norovirus [15].

Long-term efficacy is essential for daily touch surfaces. On one hand, bulk copper can be regarded as a self-healing antimicrobial touch surface. It is not difficult to imagine if the top layer of copper is destroyed, the newly-exposed surface, which is still copper, which has the same antibacterial property as the original one. This ensures no substantial damage can be induced by daily touching, cleaning or even scratching. However, oxidation of copper is not neglectable [16]. Its two regular oxides: cuprous oxide (Cu_2O) and cupric oxide (CuO) have also been revealed to have relatively weaker antimicrobial activity [17]. Therefore, some other ongoing studies also began to produce corresponding oxides on copper (and its alloys) [18], in order to better evaluate the changes in antibacterial performance as well as the role of oxides.

Another relevant concern is related to the methods applied to study surface antimicrobial efficacy. In these tests, microbes need to be transferred onto the coupons together with buffer solutions, which in most of the cases are, designed to cover the tested surfaces for the whole experimental periods [19]. The presence of these buffers could cause additional effects on the surface, which have been seldom addressed or considered in the existing research.

Phosphate-buffered saline (PBS) is one of the widely used physiological buffers in many microbiological and antibacterial studies [20-22]. In this buffer, disodium phosphate (Na_2HPO_4) or monosodium phosphate (NaH_2PO_4) helps to stabilise a pH of 7.4, when sodium chloride (NaCl) ensures a suitable osmotic pressure for microbes. However, these functions do not always secure a fair antimicrobial surface test. There are still two criteria should be further considered: first, does this buffer represent the specific environment where the surface is applied? Second, does it play a neutral role, or will it instead bring additional effects into the test system, altering its original state and hence the antimicrobial performance of the surface?

To fulfil better the first criterion, artificial perspiration has been applied to simulate the scenario of daily touch surfaces in a few research [23, 24]. However, the second criterion itself is somewhat contradictory, especially in the case of copper surface. Continuous release of the antibacterial copper ion implies the original surface is undergoing chemical changes, which in many circumstances are, accomplished by corrosion attacks. However, these attacks generally not just cause dissolution of

the metallic surface, but also the formation of corrosion products. In this case, growth of copper oxides become foreseeable.

Considering the corrosion attacks on copper, they have been abundantly investigated over the past decades. To analyse these attacks induced by PBS, certain known aspects are worth being briefly mentioned. First of all, it is the reactants that promote corrosion in the neutral condition as that in PBS. Dissolution of copper is mainly promoted by dissolved oxygen instead of hydrogen ion [25]. However, PBS contains chloride ion (Cl^-), which is a reactive species that especially promotes pitting corrosion [26]. Its existence also brings the possibility of more complex intermediate/final corrosion products such as copper chloride (CuCl) or dicopper chloride trihydroxide ($Cu_2(OH)_3Cl$) which could develop into different scenarios in pitting corrosion [27]. Pits themselves, have the bright side for microstructures studies, simply because dislocations are found to be the preferential pitting sites for most of the time [28]. For the same reason, localised corrosion attacks at grain boundaries and twin boundaries were also investigated [29], where high angle and incoherent grain boundaries are found to be corroded more easily. Meanwhile, grain orientation affects the corrosion resistance of the neighbouring boundaries [30, 31]. Furthermore, under certain electrochemical conditions, etch pits occur on different grains are found to have crystallographic features, which can also be highly related to the orientation of grains [32].

Another aspect of the corrosion phenomena is the oxide growth. Analysis of this process enhances understanding of the (electro)chemical reactions involved. Usually, they are confirmed and further analysed by multiple phase analysis methods or electrochemical tests [33]. However, the microscale details of the growth process itself seldom draw attention in the currently existing research. To best our knowledge, there are only a few studies that mentioned the epitaxial growth of Cu_2O on copper in aqueous environment [34], or deposition of epitaxial Cu_2O crystal in copper contained solution [35]. The focus of these investigations is the confirmation of orientation relationships that have also been previously reported in oxidation at elevated temperature [36, 37], instead of the relevant corrosion processes.

Our recent study has reported the localised corrosion attacks directly found on ground copper, since oxide growth is inhibited by the accumulation of copper in bacteria [38]. Therefore in the current study, more details from the corrosion aspect are revealed. In the first part of this work, we first revisited the corrosion sites on ground copper induced by PBS, but with another method, namely backscatter electron imaging. And then, the focus was diverted to both the localised corrosion attacks and oxide growth on mainly on electropolished copper. Additional ex-situ characterisations such as electron backscatter diffraction was conducted. Various results from enable us to describe the detailed features of corrosion sites such as intergranular attack, crystallographic etching and other corrosion sites on grains with certain preferential orientations. Moreover, the epitaxial growth of copper oxide growth has also been recorded and analysed. Based on these results, the second part of the work applied *E. coli* PBS suspension for comparison, where the roles of bacteria on corrosion behaviours on copper were further discussed.

2. Materials and methods

2.1. Materials

Copper (99.99%, K09, Wieland) was chosen for both types of coupon: ground and electropolished. Ground coupons were mechanically ground with silicon carbide sandpaper (stepped down to grit number P600). Electropolished coupons were firstly mechanically ground and polished, finishing with 1 μm diamond paste, and cleaned with soap. Importantly, these coupons were electropolished in 85 wt% orthophosphoric acid (2 V, 3 min). After these grinding or polishing procedures, both types of coupon were rinsed with water, cleaned with ethanol in an ultrasonic bath, and dried by air.

2.2. Solutions

The preparation of PBS (0.01 M NaH_2PO_4. $1H_2O$, 0.14 M NaCl, pH about 7.4) and PBS with *E. coli* K12 can be referred to our recent publication [38]. For the bacterial suspension, the initial average cell count was around 3×10^9-5×10^9 CFU/ml.

2.3. Corrosion protocol

To introduce corrosion on copper coupons, droplet exposure method (instead of immersion) was applied, in order to be kept as similar as the antibacterial efficiency tests performed in our other works [17, 39]. In brief, 20 μL of PBS or *E. coli* PBS suspension were applied on coupons with a pipette. These coupons were placed in a water-saturated atmosphere at room temperature. After certain exposure time (1 h, 3 h and 6 h), these solutions were withdrawn and the coupons were further cleaned with ethanol in an ultrasonic bath.

To remove the corrosion products from the coupon surface, acid etching was used. Coupons were immersed in 4 wt% hydrochloric acid (10 s), rinsed with water rinse and cleaned with ethanol in an ultrasonic bath.

2.4. Surface characterization

Different functions of scanning electron microscope (SEM, Helios NanoLab600, FEI) were applied to observe copper surfaces after various corrosion experiments. Secondary electron detector (SE) was applied to describe the top-surface as well as cross-section of the coupons, while backscatter electron detector (BSE) depicted localised corrosion attacks exposed or covered by corrosion products. Acceleration voltages will be further mentioned in the corresponding figure captions. Transmission electron microscope lamella was prepared by focused ion beam (FIB) and finally attached on copper grid, so that scanning transmission electron microscopy mode (STEM) can be carried out at 30 kV, in order to survey the details of corrosion products. To investigate the orientation relationship between the corrosion products and the substrates underneath, electron backscatter diffraction patterns (EBSD) were collected with step sizes of 200 nm (for fine scan at small regions) or 1 μm (for rapid scan at droplet edges) at 20 kV. Optical microscope (OM, OLS4100, Olympus) photos were captured in 3D bright field mode to so that the colours induced by the corrosion products can be preserved. For further confirmation of these corrosion products covering the surfaces, Raman spectroscopy (Raman, operating at 633 nm, inVia, Renishaw) with a 50X OM and

high resolution grazing incidence X-ray diffractometer (GIXRD, Cu Kα with 1° grazing angle, PANalytical X'Pert PRO-MPD) were applied. All these images and spectra were obtained within 24 h after the corresponding treatments.

2.5. Copper content determination

For the coupons to be measured, 10 µL samples were withdrawn by repetitive pipetting in the end of the corrosion protocol. To prepare the final samples for inductively coupled plasma mass spectrometry (ICP-MS, 7500cx, Agilent) measurement, they were first diluted in 2.990 mL 1 wt% nitric acid (Merck, Germany). Afterward, 3 µl of 10 mg/l scandium and caesium internal standard solutions were added to the samples. For calibration, standards with 0.1, 0.5, 2.5, 10, 50, 250 and 1000 µg/L of copper were used. The original results with a unit of ppb were converted to the final values with µmol/L (µM), considering the fold of dilutions and molar mass 63.55 g/mol for copper. Results from ICP-MS represent the sum of every type of copper form presented in the samples. The average values and standard deviations were obtained by three independent experiments.

3. Results and discussion

3.1. From ground copper to electropolished copper: localised corrosion attack, oxide growth and copper release

Growth of Cu_2O on ground copper was observed in PBS, which has been preliminarily discussed in our previous study [38]. Here, special emphasis is placed on the copper substrate underneath. To obtain information not only from the outer oxide layer but also from the copper substrate covered, higher acceleration voltage (20 kV instead of 5 kV) was employed in SEM. From the SE images shown in Figure 1 (a-c), the growth of oxide as a function of time is observed by the change of microscale topography. They are not as evident as the scratches, since an electron beam with higher incident energy produces secondary electrons from a larger and deeper region of the sample, weakening the fine topographic contrast [40].

Nevertheless, there are dark dot-like zones that become visible. They become much more obvious in the BSE images shown in Figure 1 (d-f). The size of these dots gradually increased as the corrosion prolonged from 1 h to 3 h. But when it extended to 6 h, they are hard to be located. Based on the origins of BSE contrast and the fact that no inclusion should be introduced during the corrosion process, it is thus suggested that each of these dark zone represents a cavity beneath the oxide coverage, as a result of localised corrosion attack. Increase of these cavities in size implies that pitting continued. In the meantime it is this corrosion process that allows the release of copper into solution. On the other hand, missing of these cavities in 6 h could be ascribed to a few causes. Firstly, it is clear that the oxide layer was getting thicker as a function of time, as a higher acceleration voltage is needed to detect the corrosion spots (SEM images in SI Figure 1). Secondly, oxide could also grow inside these cavities, in another word, filling the cavities from inside (Raman spectra in SI Figure 1).

Another important fact of these pits are their non-random distribution: along the scratches seems to be favourable

locations. Scratches that are introduced in grinding procedure do not simply represent height difference but also inhomogeneity of microstructure such as finer grain sizes and internal stress. Therefore this phenomenon is consistent with the previous study revealing pits distributed along dislocations [28]. That is to say, the state of copper surface has a huge influence on its corrosion behaviour, and in this case, the positions where pits initiate. As ground copper is always reported being covered by a deformed layer [41], it makes further analysis difficult if the aim is to comprehensively understand the correlation between the microstructure and the corrosion behaviours in PBS.

Therefore, electropolished copper were prepared, so that distinguishable grains could be revealed. Typical SE and BSE images of these coupons are displayed in Figure 2. At the beginning of corrosion (1h), different "blocks" can be distinguished in the SE micrograph, indicating that grains were somehow corroded differently, leading to a topographic contrast. This contrast becomes ignorable as time goes by, since oxide layer began to form on all these grains covering those corrosion sites on grains. Results from BSE show a similar trend, but the origin of the contrast shown on 1 h coupon is different: it is mainly ascribed to the strong electron channelling effect of the copper grain orientation [40]. When it comes to the cavities (darker zones in BSE), their dimension kept increasing from 1 h to 6 h, symbolising continuous pit growth. Meanwhile, their locations were more regular: most of them are found along the copper grain boundaries, a sign of the initiation of intergranular attack.

Oxide layer on these electropolished coupons was growing thicker as well. To observe the pits underneath, low acceleration voltage is not sufficient anymore for the long time corrosion coupons (SI Figure 2). Besides, the oxide grown on these coupons has its own characteristic compared to the one grown on ground copper. Typical cross-sectional SE images of these two coupons after 6 h corrosion are compared in Figure 3 (a) and (b). Oxide layer on ground copper is relatively homogeneous in thickness, following the substrate topography. In the case of electropolished copper, first of all, the aim of electropolishing protocol is confirmed, as a sharp edge with relatively low roughness copper surface is found. Secondly, this edge selected here as the copper-oxide interface is found still intact after corrosion. Furthermore, oxide grown on electropolished copper shows a particular phenomenon less visible on ground copper due to the absence of near-surface deformed layer: the thickness of oxide seems to highly depend on the copper grain underneath.

Since FIB cross-sections are always too local and thus may lack of statistics, OM was applied to provide macroscopic details. The colour of these oxides in OM highly and mainly depends on their thickness as a result of interference [42]. Therefore these OM photos (Figure 3 (c-e)) suggest the localised similarity of the oxide thickness. Moreover, the intensity of oxide signal shown in GIXRD results could be regarded as a qualitative index of the oxide amount. In Figure 3 (f) and (g), {111} diffraction peaks were compared since they are the most observable peaks for such a small amount of substance. It is obvious that the sum of oxide grown on electropolished copper was less (means slower) than that grown on ground copper.

Corrosion not only introduces chemical changes on the surface, but also influences the environment, which is the solution in this case. For example, copper content that released and entered the solution, which is usually positively correlated with

the antibacterial efficiency shown [17], could also tell the chemical interaction along the time. As shown in Figure 4, the copper concentration in the droplet that contacted with electropolished coupons did not go through a decline phase as that with ground coupons. This phase could imply the occurrence of oxide coverage, which consumed copper ions by its formation, and at the same time, acted as a barrier stopping copper from direct release. However, owing to the exposure of distinct copper grains on electropolished coupon, oxide growth became more grain-dependent and therefore less homogeneous. One of the consequences is that it takes a longer time for some certain grains to be fully covered by oxide. Therefore before this moment, copper ion is allowed to be released directly. On the other hand, the ground copper released almost twice more copper ion in 1 h. This could mean that the electropolished copper actually has relatively higher corrosion resistance. It further implies that intergranular corrosion also dominate on ground coupons, since the existence of highly deformed layer is consisted of finer grains and a higher boundary density.

3.2. Re-deposition of oxide on copper grains

Since the oxide grown on electropolished copper has its distinct features, much attention is now drawn by it. For example, Figure 5 presents some higher resolution micrographs of the oxide layer. Above all, boundaries exist among these oxides. Different parts of the oxide not only have various contrast but also vary in sub-micron roughness/topography. If one looks carefully, it can be found that this slight difference is caused by the very fine facet-like features. These features are more distinguishable in those STEM images. The shapes of oxide on one grain are found to follow the same pattern. This pattern exists not just on the front side that was exposed directly by FIB (profiled red), it is also true for the other parts (profiled blue) that were covered by the Pt protection layer. And again, the copper grain shown here under the oxide seems to be still intact.

To better understand the oxide grown on electropolished copper in terms of its microstructure, EBSD was performed near the trace of droplets. Inverse pole figure (IPF) maps of coupons after 1 h and 6 h corrosion test are shown in Figure 6 (a) and (c), respectively. It is clear that the edge of the droplet divides two regions that each has its own distinct orientation distribution. Although it has to be noted that, on the 1 h coupon, the orientation information on the droplet side may not simply represent the oxide layer. As shown in SI Figure 3, the confidence index (CI) on the droplet side is much lower (and therefore darker). This CI indicator thus tells two facts: first, oxide layer grown in 1 h was still very thin, therefore EBSD detector also collected the Kikuchi patterns from the copper substrate below; second, similarity between the crystal structures of Cu_2O and copper leads to two similar sets of Kikuchi lines. The origins of these superposed diffractions are undistinguishable for the software. The CI values improve as the oxide grew thicker, implying that only Kikuchi lines from the upper part of the oxide layer was collected.

Back to the IPF maps, there is no doubt that sort of preferential oxide growth appeared, as the orientations presented by colours such as green, yellow and blue become predominant on the droplet side. For the present, it seems more reasonable to call those oxides sharing a similar orientation as a “pseudo oxide grain”, since it is not easy to tell from definition whether

they really belong to one grain (see SI Figure 4). Still, it is worth to mention that these pseudo oxide grains do not differ too much from the copper grains (outside the droplet) in size. This feature, together with the above STEM results, suggest certain crystallographic relationships may exist between the oxides and the copper substrate beneath.

To investigate this potential relationship, it is necessary to remove the oxide so as to obtain information from the copper grains underneath, which was accomplished by hydrochloric acid etching. EBSD of the same coupons at the same locations were obtained, whose IPF maps are shown in Figure 6 (b) and (d). Comparing the regions outside the droplet with their un-etched state, only a small orientation drift is nevertheless inevitable because the extremely exact sample mounting is not possible. On the other hand, the former droplet side share a similar orientation distribution as the outer regions, confirming that the etching is sufficient thus it was the copper substrate that already exposed.

From a rough comparison amid Figure 6, it is obvious that below almost every pseudo oxide grain there is a corresponding copper grain. To further investigate their orientation relationships, distribution of four certain crystal directions were chosen and re-drawn in Figure 7, with certain degrees as tolerance. Their correspondences are considerably clear: the reason why "blue blocks" in IPF become dominant is that except from Cu_2O {111} preferential grown on Cu {111}, it is also common to find out Cu_2O {111} on Cu {001}. For the same reason, due to other two relationships, namely Cu_2O {101} // Cu {101} and Cu_2O {101} // Cu {113}, "green blocks" become popular too.

Similar orientation relationships have been reported when Cu_2O was found growing on copper single crystal in elevated temperature [36, 37]. This is mainly attributed to the low misfit of copper atom positions in the interface between two phases. However, in those circumstances, growth of oxide depends on a series reactions such as capture of oxygen species, reconstruction of interface, further growth through diffusion of oxygen or oxygen vacancies, etc. [43] Also, there are usually two consistently moving oxide fronts: the side exposed to the air and the oxide-metal interface, not just the former one shown in our STEM results. In addition, this type of epitaxial growth was also found on copper single crystal when it was immersed in a copper contained solution where further considered as a deposition process [35].

These relevant examples are helpful for understanding the current study. The solution applied (PBS) for sure does not contain any copper species in the beginning, however, it becomes a copper contained solution once corrosion happens and copper ion is released. Afterwards, the process can be described similar to the epitaxial growth in thin films fabrication [44]. Firstly, copper oxide nucleus are formed. These nucleation centres are tiny, separate but sharing the same crystal orientation with those who are also growing on the same copper grain. They keep growing as long as the copper ion in the solution is adequate, and finally merge with each other, becoming seemingly a pseudo grain. From the current EBSD results, this type of growth is also statistically confirmed. From this perspective, the reason why thickness of oxides differ from grains can also be explained: the growth rates are also orientation-dependent, i.e. grain-dependent. To sum up, the formation of Cu_2O on electropolished copper in PBS is a re-deposition process, accomplished by the copper ions presented in the solution, rather

than a classical direct oxidation of the metallic surface in elevated temperature conditions.

3.3. Localised corrosion attacks on specific microstructures

Now that the oxide layer has been removed, an opportunity to check the corrosion sites on copper surface is provided. A localised EBSD scan was performed with a finer step size for the 6 h corrosion coupon and various forms of this result are shown in Figure 8. For example, image quality (IQ) map is an effective way to present the locations of pits or cavities, since these areas have less clear Kikuchi patterns, i.e. worse image quality. Combining carefully with the grain boundary map (possible obstacles see SI Figure 5), it is clear that intergranular corrosion occurs at both twin boundaries and other grain boundaries. However, only small proportion of twin boundaries was found attacked, while other boundaries seem to be more susceptible to the corrosion attacks. Former research has suggested that low angle grain boundaries and coherent/twin boundaries have higher corrosion resistance in Cl^- contained solution [29]. It is, nevertheless, fair to claim that only the latter preference is observed in this study, because the proportion of low angle boundaries are relatively low and may not show the general trend even there is one.

Moreover, removal of oxide layer helps to find out the corrosion sites within grains as well. It happens to be less obvious on grains with regular Miller index planes ({001}, {101} and {111}) parallel to the surface. On the contrary, for most of the grains suffering severe corrosion, they tend to share a closed crystal direction to {102}. However, it is also true that grain-dependent corrosion may not be simply related to the grains themselves: studies using in-situ scanning electrochemical microscopy (SECM) found out that the tip current measured on grains, which could symbolise the corrosion resistance, were also determined by the neighbour grains [30, 31]. Scanning electrochemical cell microscopy (SECCM) can be a promising method for the future work, since the electrolyte can be spread only on a single grain [45], so that the likely influences from the neighbour grains should be isolated.

Moreover, high resolution SEM images (Figure 8 (c-d)) provide details of the corrosion sites in terms of their shapes: SE images tell the bare facets exposed inside a cavity, while BSE images highlight the appearance of cavity itself. It is easily found that both these shapes follow certain patterns, reflecting the crystal direction of the grains they belong to (Figure 8 (e)). This implies a result of crystallographic corrosion/etching, where the most dissolvable crystallographic planes were left and exposed [32, 46], and thus the shape of a cavity highly depends on the grain orientation. Identifying this mechanism helps to know better how preferential corrosion occurs as a quasi-two-step process. The first step is the initiation of the corrosion. Take grain boundaries as an example, they are generally believed to be less stable therefore favourable to corrosion. But once these unstable regions are corroded away, the rest are the relatively perfect grains on both side of the original boundaries. However, corrosion does not necessarily stop, it could widen the cavity, not due to the unstable regions, but crystallographic corrosion. Therefore reactants (Cu^{2+} & Cl^-) and pH inside pits which are usually different from the bulk solution, should play an assistant role in this step. Otherwise global nucleation of corrosion sites should have been observed, instead of the sustained

developing of the existent attacked sites.

Since corrosion sites are always lower than the original surface, this means that these locations may not always be available for EBSD analysis. On one hand, due to the topographical shadow effect (projection effect), the corresponding relationship between the actual regions and patterns received may not match. On the other hand, the quality of Kikuchi patterns could worsen, therefore the orientation information of certain positions cannot be correctly identified by the software. Consequently, to compare and identify Kikuchi patterns manually could be a meaningful mean to extract those distorted information. Figure 9 shows a region mainly composed by three identified grains and an intergranular attack site among them. Kikuchi patterns from these three grains are clear and distinguishable, providing eligible references for the following comparison. Kikuchi patterns from three positions inside the groove, nevertheless, are with considerably worse contrast, which are as expected. Especially for position 2 and 3, a relatively large portion of EBSD camera did not receive any effective signal and thus looks completely dark. The reason is that those Kikuchi lines generated were blocked by the "cliff" of grain C. However, to carefully compare the recorded parts, one could still find out that all these three positions should be identical to each other, and most importantly, can be classified as part of the pattern obtained from grain A. That is to say, although the so-called intergranular corrosion initiated in the grain boundary, the further expansion of the pit could be grain-preferential and therefore anisotropic, probably owing to the localised galvanic corrosion between two grains. In this case, the exposed surface is in fact part of grain A, suggesting that grain A was acting as anode for the whole corrosion period, thus suffering from most intense dissolution. Grain B and grain C, on the other hand, were cathodic sites and free from corrosion. These details are also the evidence of how neighbour grains could influence the tendency of intergranular attack.

3.4. Corrosion phenomena in *E. coli* PBS suspension

Thus far, we have obtained fundamental information from the copper-PBS system, which further fosters understanding in the corrosion phenomena when *E. coli* are presented. As shown in Figure 10 (a), localised attack is the most common type of corrosion found in this circumstance. These pits are following the similar distribution as those identified on PBS corroded coupon (originally shown in Figure 1). On electropolished copper, Figure 10 (b) and (c) also show similar corrosion sites as those introduced by pure PBS: some grains and some sections of grain boundaries were under severe attack. It should be noted that, these SEM observations were done without hydrochloric acid etching treatment, since there were almost no GIXRD detectable oxide layer formation (Figure 10 (d)). This could be attributed to the roles played by bacteria, such as accumulation of copper ions from the solution, which has been recently discussed [38]. This argument is now further supported by the re-deposition mechanism of oxide growth described in previous section in this current study: copper ions that are accumulated by the bacteria and therefore cannot be used to form oxide.

For the same reason, direct EBSD analysis of the corrosion sites becomes possible. Figure 11 demonstrates very similar details of those preferential corroded sites in the presence of *E. coli*, compared to the case of pure PBS: grain boundaries and

{102} direction grains are relatively vulnerable; obvious intergranular attack and crystallographic etching are found as well. These similar features on electropolished coupons regardless of the presence of *E. coli* are together suggesting one fact: adding *E. coli* into PBS does not significantly change the major corrosion mechanisms on copper.

However, does it mean that *E. coli* would not introduce new corrosion sites either? There are some observations shown in Figure 12 that can provide some hints. For example, except from the pits and the remained bacteria (owing to insufficient withdrawal), a huge amount of separate dark sites are found. They are different in size, but the largest ones are similar to the size of *E. coli* cell. After compared to the same feature under those bacteria remained, it is thus reasonable to deduct that these dark sites might represent the locations where the bacteria once were (i.e. before they were withdrawn). Their chemical information is unfortunately still unknown, as the BSE image already suggests its thinness, making in-situ EDS analysis not possible. However, it is much more noteworthy that the copper surface covered by these marks were not necessarily be corroded. The opposite is also true: the locations where pits appeared do not necessarily have these marks on/around them. This may verify the role of *E. coli* in the present corrosion experiment and thereby answer the abovementioned question: no new corrosion sites exclusively introduced by *E. coli* is found.

From another perspective, the existence of these dark marks convey a hidden message: *E. coli* tend to settle down and contact with the surface. It is no surprise that this happens to *E. coli* after they get killed due to the antibacterial nature of copper ion [39], and therefore lose their mobility. Although this type of contact does not show any influence in the corrosion attacks that copper endures, it does reduce the area where copper is directly exposed with solution. Oxide re-deposition could also be prevented in such a way.

Combined with other results discussed, a more comprehensive picture of antibacterial efficiency test is now shown, in terms of interplay between copper surface and bacteria in PBS environment, where corrosion should be considered as the key. On the other hand, efficient design of antibacterial surfaces should be expected based on the phenomena observed. For example, surface with finer grains contains longer grain boundary section should include more favourable corrosion sites to release antimicrobial copper ion. Preferred growth of copper thin films could also be applied to control exposed facet, resulting in a different corrosion resistance, which eventually leads to a controllable antibacterial activity. Furthermore, surfaces consisted of exposed crystallographic planes with lower oxide growth rate could inspire further designs applied in long-term application.

4. Conclusions

Chemical and morphological changes induced by PBS on copper surfaces were examined, which can be divided into two simultaneous process: localised corrosion attacks of copper surface and oxide growth on top. Some significant features and

important implications found in these two processes are summarised below.

For localised corrosion attacks:

- Pitting sites on ground copper were found along the scratches. They grew in size from 1h to 3h, but become less distinguishable in 6h.
- On electropolished copper, intergranular corrosion was the most predominant attack, where twin boundaries were less vulnerable. After an intergranular attack initiates on the grain boundaries, it can further develop in an extremely anisotropic way, probably due to localised galvanic corrosion between neighbouring grains.
- Copper grains have also shown different corrosion resistance, those suffered much attack have orientations close to {102} planes parallel to the surface. The appearance of the corrosion sites indicates the occurrence of crystallographic etching.
- *E. coli* addition in PBS did not evidently change the characteristics of above-mentioned corrosion phenomena. No correlation has been found between the corrosion sites and the positions where bacteria locate.

For oxide growth:

- After same treatment durations, fewer amount of Cu_2O has grown on electropolished copper, which was less homogeneous than on ground copper. Distinction in the copper release trend could be one of its consequence.
- On electropolished copper, growth of Cu_2O can be regarded as an epitaxial re-deposition process, which leaded to a grain-dependent growth rate as well as a distinct difference in sub-micron surface morphology.
- Four pairs of obvious orientation relationships were found, namely Cu_2O {111} // Cu {001}, Cu_2O {111} // Cu {111}, Cu_2O {101} // Cu {101} and Cu_2O {101} // Cu {113}, suggesting that it was the misfit of copper atom positions that mainly determine this re-deposition process.
- With addition of *E. coli* in PBS, oxide growth on electropolished copper was inhibited to a great extent.

Acknowledgements

This study was supported by Erasmus Mundus Joint European Doctoral Programme in Advanced Materials Science and Engineering (DocMASE, 512225-1-2010-1-DE-EMJD, European Commision) and the PhD-Track-Programme (PhD02-14, Franco-German University). The ICP-MS experiments were supported by Dr. Ralf Kautenburger from the chair of Inorganic Solid State Chemistry. The authors acknowledge Prof. Volker Presser and Leibniz Institute for New Materials for the access of Raman spectrometer. We also thank Dr. Christoph Pauly for technical support and inspirational discussion in coupon preparation and characterisation.

Declarations of interest

None.

Data availability

The data that support the findings of this study are available from the corresponding author on request.

References

[1] M.P. Muller, C. MacDougall, M. Lim, I. Armstrong, A. Bialachowski, S. Callery, W. Ciccotelli, M. Cividino, J. Dennis, S. Hota, G. Garber, J. Johnstone, K. Katz, A. McGeer, V. Nankoosingh, C. Richard, M. Vearncombe, Antimicrobial surfaces to prevent healthcare-associated infections: a systematic review, Journal of Hospital Infection, 92 (2018) 7-13.

[2] M. Vincent, R.E. Duval, P. Hartemann, M. Engels‐Deutsch, Contact killing and antimicrobial properties of copper, Journal of Applied Microbiology, 124 (2018) 1032-1046.

[3] R.J. Turner, Metal‐based antimicrobial strategies, Microbial Biotechnology, 10 (2017) 1062-1065.

[4] S.L. Warnes, S.M. Green, H.T. Michels, C.W. Keevil, Biocidal Efficacy of Copper Alloys against Pathogenic Enterococci Involves Degradation of Genomic and Plasmid DNAs, Applied and Environmental Microbiology, 76 (2010) 5390-5401.

[5] R.K. Swarnkar, J.K. Pandey, K.K. Soumya, P. Dwivedi, S. Sundaram, S. Prasad, R. Gopal, Enhanced antibacterial activity of copper/copper oxide nanowires prepared by pulsed laser ablation in water medium, Applied Physics A, 122 (2016) 1-7.

[6] S. Shinde, H. Dhaygude, D.-Y. Kim, G. Ghodake, P. Bhagwat, P. Dandge, V. Fulari, Improved synthesis of copper oxide nanosheets and its application in development of supercapacitor and antimicrobial agents, Journal of Industrial and Engineering Chemistry, 36 (2016) 116-120.

[7] G. Sharmila, M. Thirumarimurugan, V.M. Sivakumar, Optical, catalytic and antibacterial properties of phytofabricated CuO nanoparticles using Tecoma castanifolia leaf extract, Optik - International Journal for Light and Electron Optics, 127 (2016) 7822-7828.

[8] C. Hahn, M. Hans, C. Hein, A. Dennstedt, F. Mücklich, P. Rettberg, C.E. Hellweg, L.I. Leichert, C. Rensing, R. Moeller, Antimicrobial properties of ternary eutectic aluminum alloys, BioMetals, (2018).

[9] Y. Kang, J. Park, D.-W. Kim, H. Kim, Y.-C. Kang, Antibacterial and physicochemical properties of co-sputtered CuSn thin films, Surface and Interface Analysis, 50 (2017) 138-145.

[10] A. Javid, M. Kumar, S. Yoon, J.H. Lee, J.G. Han, Size-controlled growth and antibacterial mechanism for Cu:C nanocomposite thin films, Physical Chemistry Chemical Physics, 19 (2017) 237-244.

[11] Y. Sun, V. Tran, D. Zhang, W.B. Wang, S. Yang, Technology and Antimicrobial Properties of Cu/TiB2 Composite Coating on 304 Steel Surface Prepared by Laser Cladding, Materials Science Forum, 944 (2019) 473-479.

[12] V.M. Villapún, C.C. Lukose, M. Birkett, L.G. Dover, S. González, Tuning the antimicrobial behaviour of Cu85Zr15 thin films in “wet” and “dry” conditions through structural modifications, Surface and Coatings Technology, 350 (2018) 334-345.

[13] G.I. Nkou Bouala, A. Etiemble, C. Der Loughian, C. Langlois, J.F. Pierson, P. Steyer, Silver influence on the antibacterial activity of multi-functional Zr-Cu based thin film metallic glasses, Surface and Coatings Technology, (2017).

[14] S.L. Warnes, V. Caves, C.W. Keevil, Mechanism of copper surface toxicity in Escherichia coli O157:H7 and Salmonella involves

immediate membrane depolarization followed by slower rate of DNA destruction which differs from that observed for Gram-positive bacteria, Environmental Microbiology, 14 (2012) 1730-1743.

[15] S.L. Warnes, C.W. Keevil, Inactivation of Norovirus on Dry Copper Alloy Surfaces, PLoS ONE, 8 (2013) e75017.

[16] I. Platzman, R. Brener, H. Haick, R. Tannenbaum, Oxidation of Polycrystalline Copper Thin Films at Ambient Conditions, The Journal of Physical Chemistry C, 112 (2008) 1101-1108.

[17] M. Hans, A. Erbe, S. Mathews, Y. Chen, M. Solioz, F. Mücklich, Role of Copper Oxides in Contact Killing of Bacteria, Langmuir, 29 (2013) 16160-16166.

[18] M. Walkowicz, P. Osuch, B. Smyrak, T. Knych, E. Rudnik, Ł. Cieniek, A. Różańska, A. Chmielarczyk, D. Romaniszyn, M. Bulanda, Impact of oxidation of copper and its alloys in laboratory-simulated conditions on their antimicrobial efficiency, Corrosion Science, 140 (2018) 321-332.

[19] H. Kawakami, K. Yoshida, Y. Nishida, Y. Kikuchi, Y. Sato, Antibacterial Properties of Metallic Elements for Alloying Evaluated with Application of JIS Z 2801:2000, ISIJ International, 48 (2008) 1299-1304.

[20] S. Wu, S. Altenried, A. Zogg, F. Zuber, K. Maniura-Weber, Q. Ren, Role of the Surface Nanoscale Roughness of Stainless Steel on Bacterial Adhesion and Microcolony Formation, ACS Omega, 3 (2018) 6456-6464.

[21] G. Wang, H. Feng, L. Hu, W. Jin, Q. Hao, A. Gao, X. Peng, W. Li, K.-Y. Wong, H. Wang, Z. Li, P.K. Chu, An antibacterial platform based on capacitive carbon-doped TiO2 nanotubes after direct or alternating current charging, Nature Communications, 9 (2018) 2055.

[22] D. Wojcieszak, M. Mazur, D. Kaczmarek, P. Mazur, B. Szponar, J. Domaradzki, L. Kepinski, Influence of the surface properties on bactericidal and fungicidal activity of magnetron sputtered Ti–Ag and Nb–Ag thin films, Materials Science and Engineering: C, 62 (2016) 86-95.

[23] L.L. Foster, M. Hutchison, J.R. Scully, Corrosion of Cu-5Zn-5Al-1Sn (89% Cu, 5% Zn, 5% Al, 1% Sn) Compared to Copper in Synthetic Perspiration During Cyclic Wetting and Drying: The Fate of Copper, Corrosion, 72 (2016) 1095-1106.

[24] D.J. Horton, H. Ha, L.L. Foster, H.J. Bindig, J.R. Scully, Tarnishing and Cu Ion release in Selected Copper-Base Alloys: Implications towards Antimicrobial Functionality, Electrochimica Acta, 169 (2015) 351-366.

[25] B. Beverskog, I. Puigdomenech, Revised Pourbaix Diagrams for Copper at 25 to 300°C, Journal of The Electrochemical Society, 144 (1997) 3476-3483.

[26] S.M. Mayanna, T.H.V. Setty, Role of chloride ions in relation to copper corrosion and inhibition, Proceedings of the Indian Academy of Sciences - Section A, 80 (1974) 184-193.

[27] A. El Warraky, H.A. El Shayeb, E.M. Sherif, Pitting corrosion of copper in chloride solutions, Anti-Corrosion Methods and Materials, 51 (2004) 52-61.

[28] L.C. Lovell, J.H. Wernick, Dislocation Etch Pits and Polygonization in High‐Purity Copper, Journal of Applied Physics, 30

(1959) 590-592.
[29] Y. Zhao, I.C. Cheng, M.E. Kassner, A.M. Hodge, The effect of nanotwins on the corrosion behavior of copper, Acta Materialia, 67 (2014) 181-188.
[30] E. Martinez-Lombardia, V. Maurice, L. Lapeire, I. De Graeve, K. Verbeken, L. Kestens, P. Marcus, H. Terryn, In Situ Scanning Tunneling Microscopy Study of Grain-Dependent Corrosion on Microcrystalline Copper, The Journal of Physical Chemistry C, 118 (2014) 25421-25428.
[31] L. Lapeire, E. Martinez Lombardia, K. Verbeken, I. De Graeve, L.A.I. Kestens, H. Terryn, Effect of neighboring grains on the microscopic corrosion behavior of a grain in polycrystalline copper, Corrosion Science, 67 (2013) 179-183.
[32] D. Landolt, R.H. Muller, C.W. Tobias, Crystallographic Factors in High‐Rate Anodic Dissolution of Copper, Journal of The Electrochemical Society, 118 (1971) 36-40.
[33] C. Toparli, S.W. Hieke, A. Altin, O. Kasian, C. Scheu, A. Erbe, State of the Surface of Antibacterial Copper in Phosphate Buffered Saline, Journal of The Electrochemical Society, 164 (2017) H734-H742.
[34] J.P.G. Farr, A.J.S. McNeil, Epitaxy in the aqueous oxidation of (001) single crystal copper films, Surface Technology, 8 (1979) 399-404.
[35] K.R. Lawless, G.T. Miller, Jnr, The epitaxial relationships of cuprous oxide formed on copper single crystals immersed in an aqueous solution of copper sulfate, Acta Crystallographica, 12 (1959) 594-600.
[36] T. Yamaguti, An Investigation on Oxidation of Crystal Surfaces with Electron Diffraction Method, II. Copper Single Crystals, Proceedings of the Physico-Mathematical Society of Japan. 3rd Series, 20 (1938) 230-241.
[37] K.R. Lawless, A.T. Gwathmey, The structure of oxide films on different faces of a single crystal of copper, Acta Metallurgica, 4 (1956) 153-163.
[38] J. Luo, C. Hein, J. Ghanbaja, J.-F. Pierson, F. Mücklich, Bacteria accumulate copper ions and inhibit oxide formation on copper surface during antibacterial efficiency test, Micron, 127 (2019) 102759.
[39] J. Luo, C. Hein, F. Mücklich, M. Solioz, Killing of bacteria by copper, cadmium, and silver surfaces reveals relevant physicochemical parameters, Biointerphases, 12 (2017) 020301.
[40] J.I. Goldstein, D.E. Newbury, J.R. Michael, N.W. Ritchie, J.H.J. Scott, D.C. Joy, Scanning electron microscopy and X-ray microanalysis, Springer, 2017.
[41] B.J. Cruickshank, A.A. Gewirth, R.M. Rynders, R.C. Alkire, In Situ Observations of Shape Evolution during Copper Dissolution Using Atomic Force Microscopy, Journal of The Electrochemical Society, 139 (1992) 2829-2832.
[42] D. Britz, A. Hegetschweiler, M. Roberts, uuml, F. cklich, Reproducible Surface Contrasting and Orientation Correlation of Low-Carbon Steels by Time-Resolved Beraha Color Etching, Materials Performance and Characterization, 5 (2016).
[43] K.R. Lawless, The oxidation of metals, Reports on Progress in Physics, 37 (1974) 231.

[44] Y. Wang, J. Ghanbaja, F. Soldera, P. Boulet, D. Horwat, F. Mücklich, J.F. Pierson, Controlling the preferred orientation in sputter-deposited Cu2O thin films: Influence of the initial growth stage and homoepitaxial growth mechanism, Acta Materialia, 76 (2014) 207-212.

[45] N. Ebejer, A.G. Güell, S.C.S. Lai, K. McKelvey, M.E. Snowden, P.R. Unwin, Scanning Electrochemical Cell Microscopy: A Versatile Technique for Nanoscale Electrochemistry and Functional Imaging, Annual Review of Analytical Chemistry, 6 (2013) 329-351.

[46] J.H. Seo, J.-H. Ryu, D.N. Lee, Formation of Crystallographic Etch Pits during AC Etching of Aluminum, Journal of The Electrochemical Society, 150 (2003) B433-B438.

Figure Captions

Figure 1

Typical SEM images of ground copper surface after 1 h **(a & d)**, 3 h **(b & e)** and 6 h **(c & f)** exposure to PBS. Same locations were imaged simultaneously with SE detector **(a-c)** and BSE detector **(d-f)** at 20 kV. All images share the same scale bars that presented in **(a)**.

Figure 2

Typical SEM images of electropolished copper surface after 1 h **(a & d)**, 3 h **(b & e)** and 6 h **(c & f)** exposure to PBS. Same locations were imaged simultaneously with SE detector **(a-c)** and BSE detector **(d-f)** at 20 kV. All images share the same scale bars that presented in **(a)**.

Figure 3

Typical SEM cross-section SE images (5 kV) of ground copper **(a)** and electropolished copper **(b)** after 6 h exposure to PBS. Typical optical micrographs obtained from the edge of the droplet traces on electropolished copper surface after 1 h **(c)**, 3 h **(d)** and 6 h **(e)** exposure to PBS. High resolution GIXRD results in the range of Cu_2O (111) planes (JCPDS#75-1531) obtained from ground copper surface **(f)** and electropolished copper surface **(g)** following various exposure periods in PBS.

Figure 4

Concentration of copper content in PBS following various exposure periods from ground copper surface (Cu_ground) and electropolished copper surface (Cu_EP). The error bars indicate the standard deviations calculated from three independent measurements.

Figure 5

High resolution SEM images of electropolished copper surface after 6 h exposure to PBS taken by SE detector **(a)** and BSE detector **(b)** at 5 kV. STEM cross-section images of the same coupon taken in: **(c)** bright field (BF), **(d)** dark field (DF) and **(e)** high angle annular dark field (HAADF).

Figure 6

EBSD results indexed and shown in the form of inverse pole figure (IPF) maps obtained from the edge of the droplet traces

on electropolished copper surface after 1 h **(a-b)** and 6 h **(c-d)** exposure to PBS. The same areas were first sampled directly after exposure **(a & c)** and then after acid etching **(b & d)**. Long dash - dot lines indicate the edge of PBS droplets. A schematic description of the treatment process and the sampled location is shown below the maps. The legend is for the above IPF maps.

Figure 7

Crystal direction (CD) maps extracted from the EBSD results obtained from the 6 h PBS treated electropolished copper surface after **(a & c)** and before **(b & d)** acid etching. The tolerance (maximum value) of misorientation angles of each CD are set as below: 10º for {001}; 15º for {111}; 12º for {113}; 15º for {101}.

Figure 8

Grain boundary networks **(a)** of electropolished copper surface after 6 h exposure to PBS and the following acid etching. Image quality (IQ) indicator and crystal direction (CD) map are combined in **(b)**, where threshold of IQ is set as 30% of the maximum measured value. High resolution SEM images of from the square region marked in **(a)** and **(b)** were taken by SE detector **(c)** and BSE detector **(d)** at 5 kV. EBSD result of the same region is shown within white dash squared in **(e)** as a combination of inverse pole figure (IPF) map and IQ map (threshold of 50%) with lattice indicators. The grey dash squared region is further presented in the following Figure 9. Legend **(a*)** for **(a)** has defined Σ3 boundary as "twin boundary", grain boundary with misorientation from 5 to 15 degrees as "low-angle boundary" and from 15 to 62.8 degrees as "high-angle boundary". The legend **(b*)** which shows tolerance (maximum value) of misorientation angles in of each CD **(b)** are set as below: 10º for {001}; 10º for {101}; 10º for {111}; 13º for {102}. **(e*)** is the legend of **(e)**.

Figure 9

SEM image (5 kV) of electropolished copper surface after 6 h exposure to PBS and the following acid etching, at a tilt angle of 70º. Same region has been indicated in Figure 8 (e). Actual or/and reconstructed Kikuchi patterns of the indicated grains (named by letters) or positions (named by numbers) are shown.

Figure 10

Typical SEM image **(a)** of ground copper surface after 3 h of exposure to *E. coli* PBS suspension. SE image **(b)** and BSE image **(c)** were taken at the same region of an electropolished copper surface after 6 h exposure to *E. coli* PBS suspension. High resolution GIXRD result in the range of Cu_2O (111) planes (JCPDS#75-1531) obtained from electropolished copper surface **(d)** following various exposure periods in *E. coli* PBS suspension.

Figure 11

Grain boundary networks **(a)** of electropolished copper surface after 6 h exposure to *E. coli* PBS suspension. Image quality (IQ) indicator and crystal direction (CD) map are combined in **(b)**, where threshold of IQ is set as 30% of the maximum measured value. High resolution SEM images of from the square region marked in **(a)** or **(b)** were taken by SE detector **(c)** and BSE detector **(d)** at 5 kV. EBSD result of the same region is shown within dash squared in **(e)** as a combination of inverse pole figure (IPF) map and IQ map (threshold of 50%) with lattice indicators. Legend **(a*)** for **(a)** has defined Σ3 boundary as "twin boundary", grain boundary with misorientation from 5 to 15 degrees as "low-angle boundary" and from 15 to 62.8 degrees as "high-angle boundary". The legend **(b*)** which shows tolerance (maximum value) of misorientation angles in of each CD **(b)** are set as below: 10º for {001}; 10º for {101}; 10º for {111}; 13º for {102}. **(e*)** is the legend of **(e)**.

Figure 12

SEM images of electropolished copper surface after 6 h exposure to *E. coli* PBS suspension were taken by SE detector **(a)** and BSE detector **(b)** at 5 kV.

Figure 1

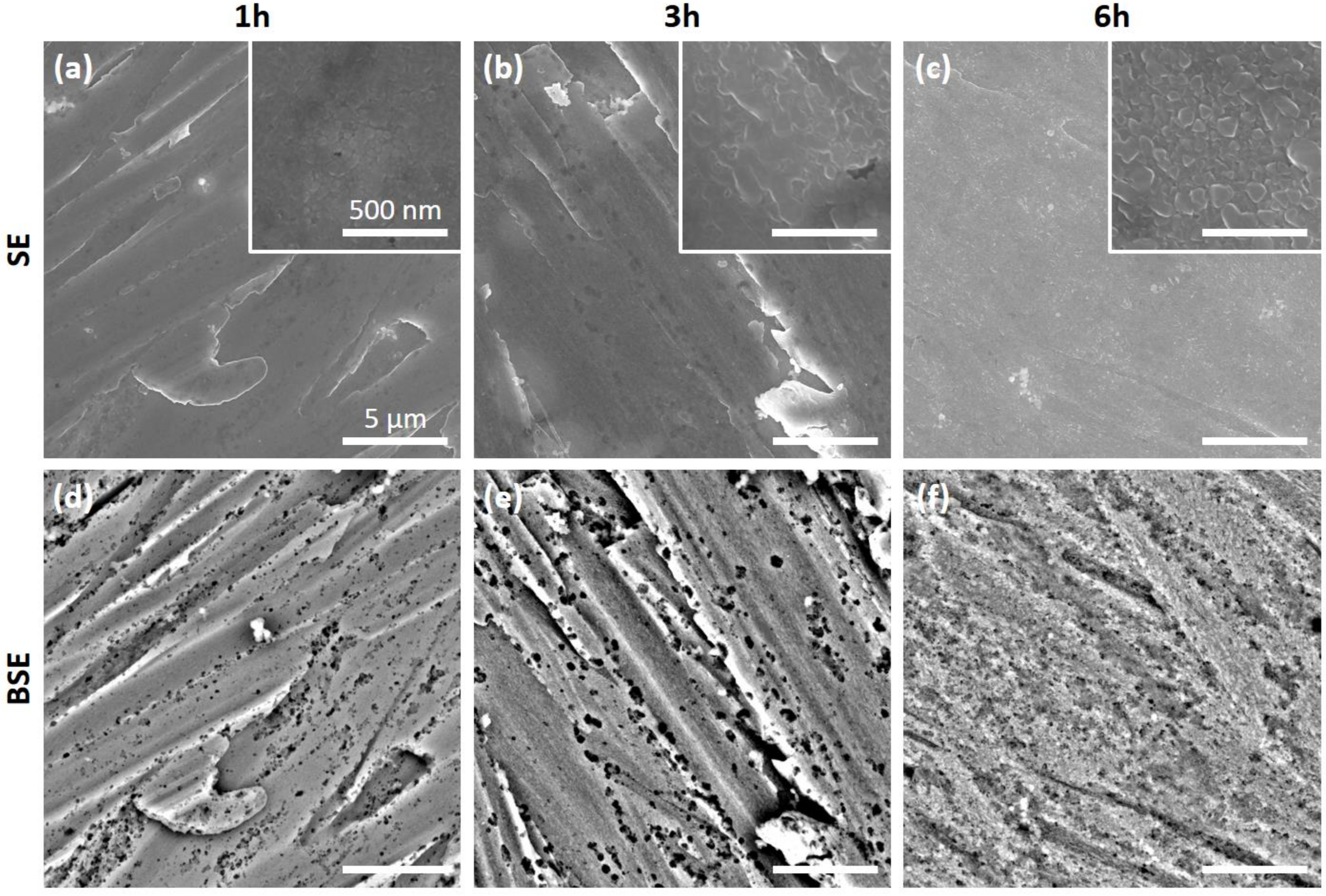

Figure 2

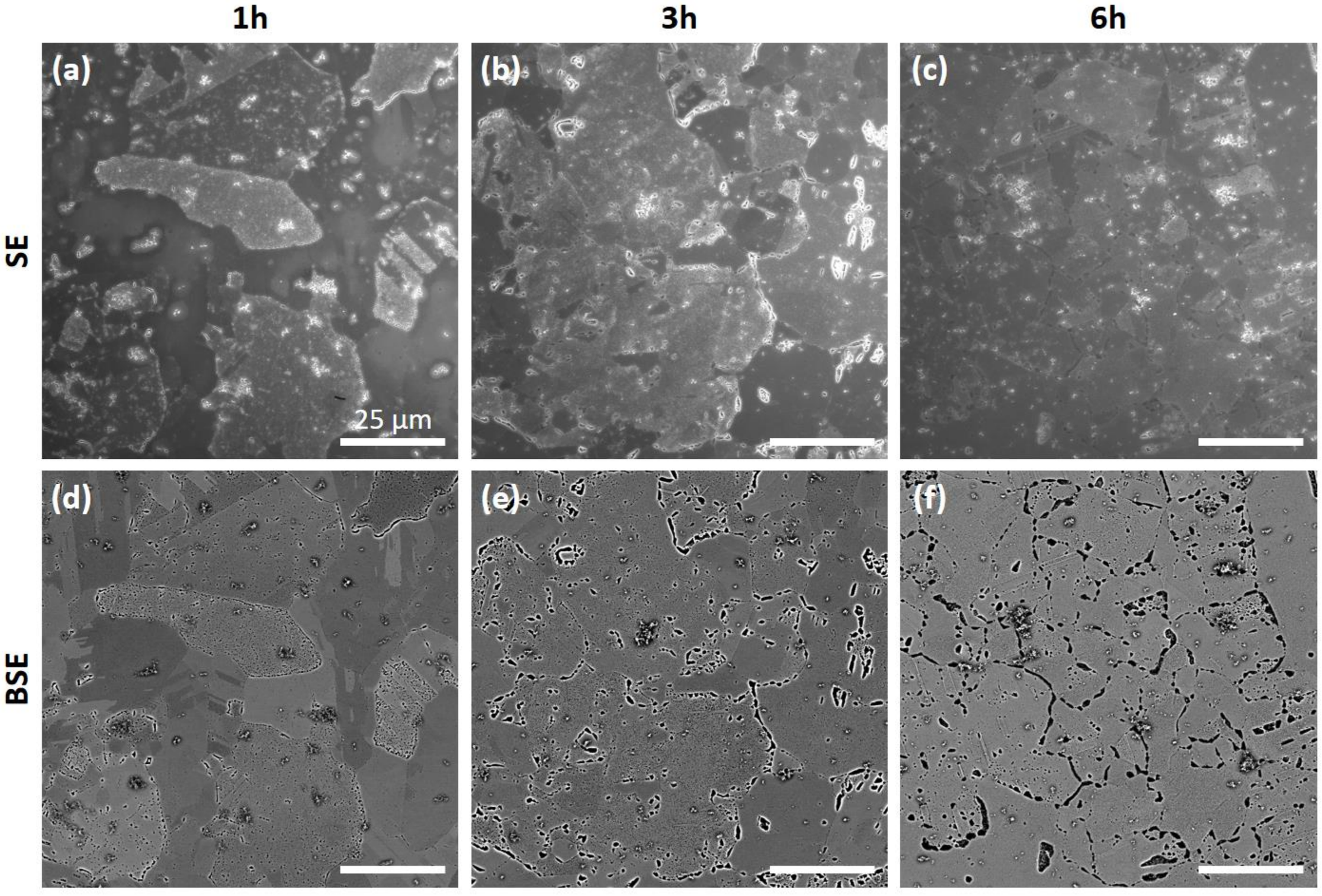

Figure 3

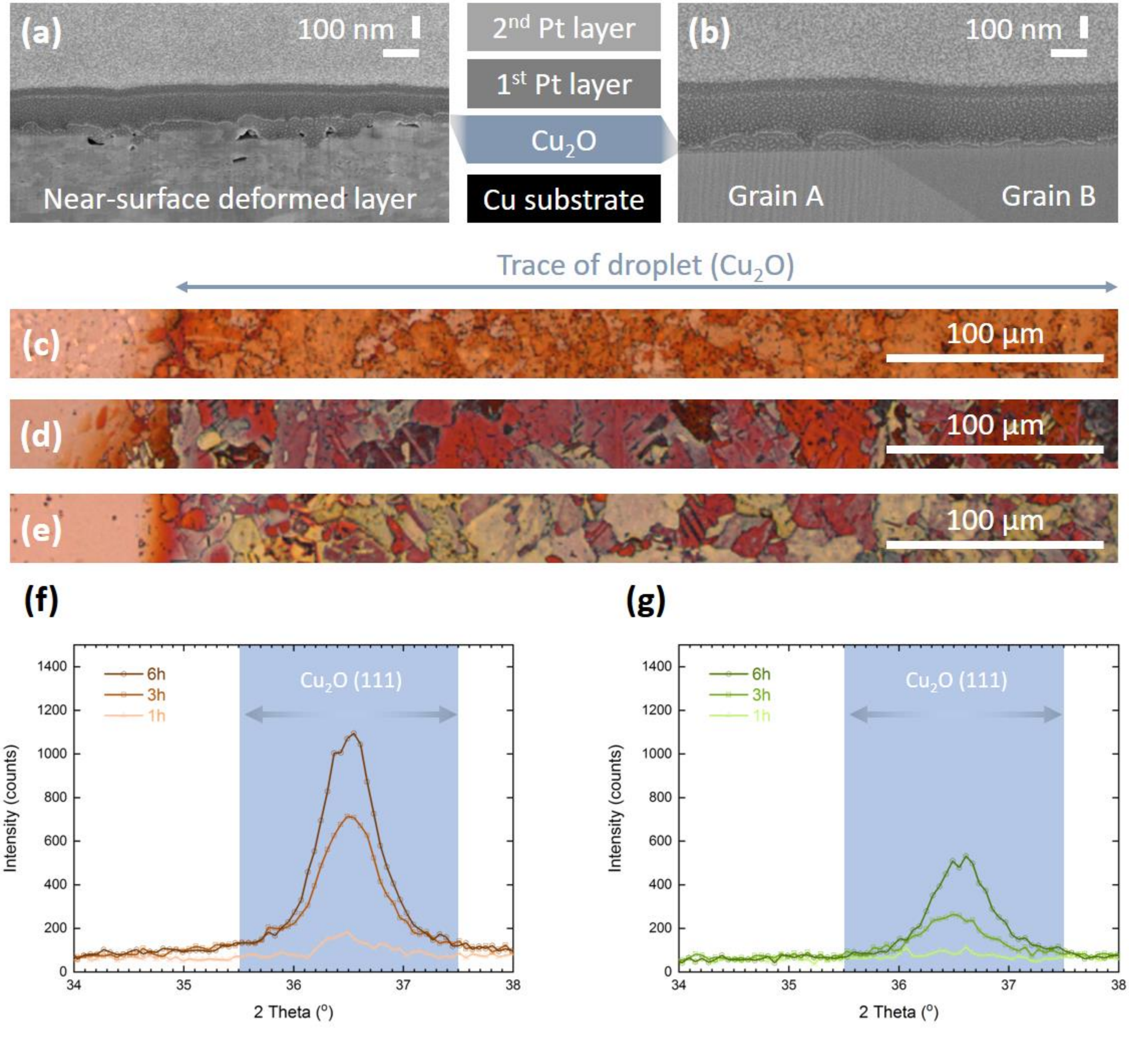
(a)
100 nm
Near-surface deformed layer
2nd Pt layer
1st Pt layer
Cu2O
Cu substrate
(b)
100 nm
Grain A
Grain B
Trace of droplet (Cu2O)
(c)
100 µm
(d)
100 µm
(e)
100 µm
(f)
6h
3h
1h
Cu2O (111)
Intensity (counts)
2 Theta (°)
(g)
6h
3h
1h
Cu2O (111)
Intensity (counts)
2 Theta (°)

Figure 4

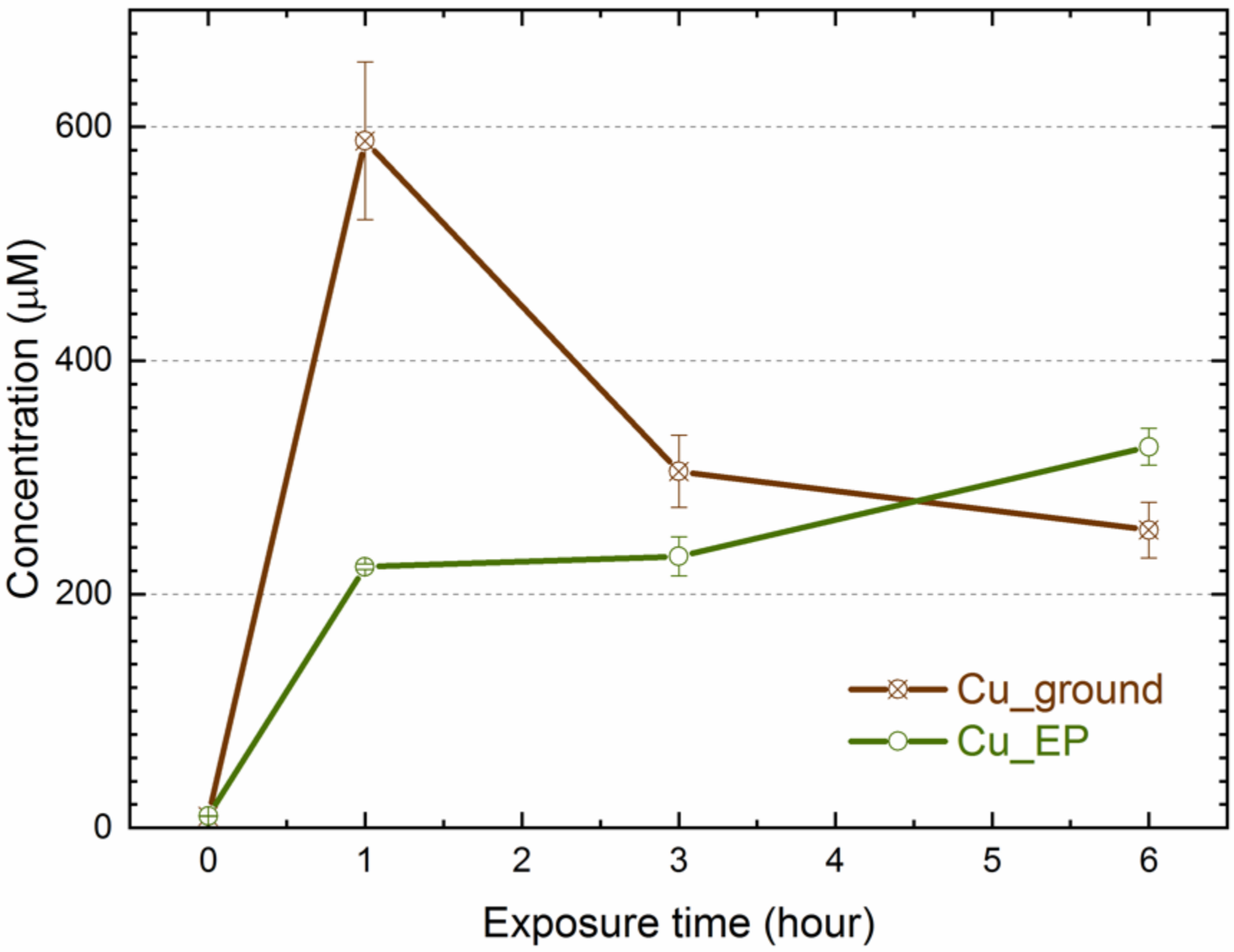
600
400
200
0
Concentration (μM)
0
1
2
3
4
5
6
Exposure time (hour)
Cu_ground
Cu_EP

Figure 5

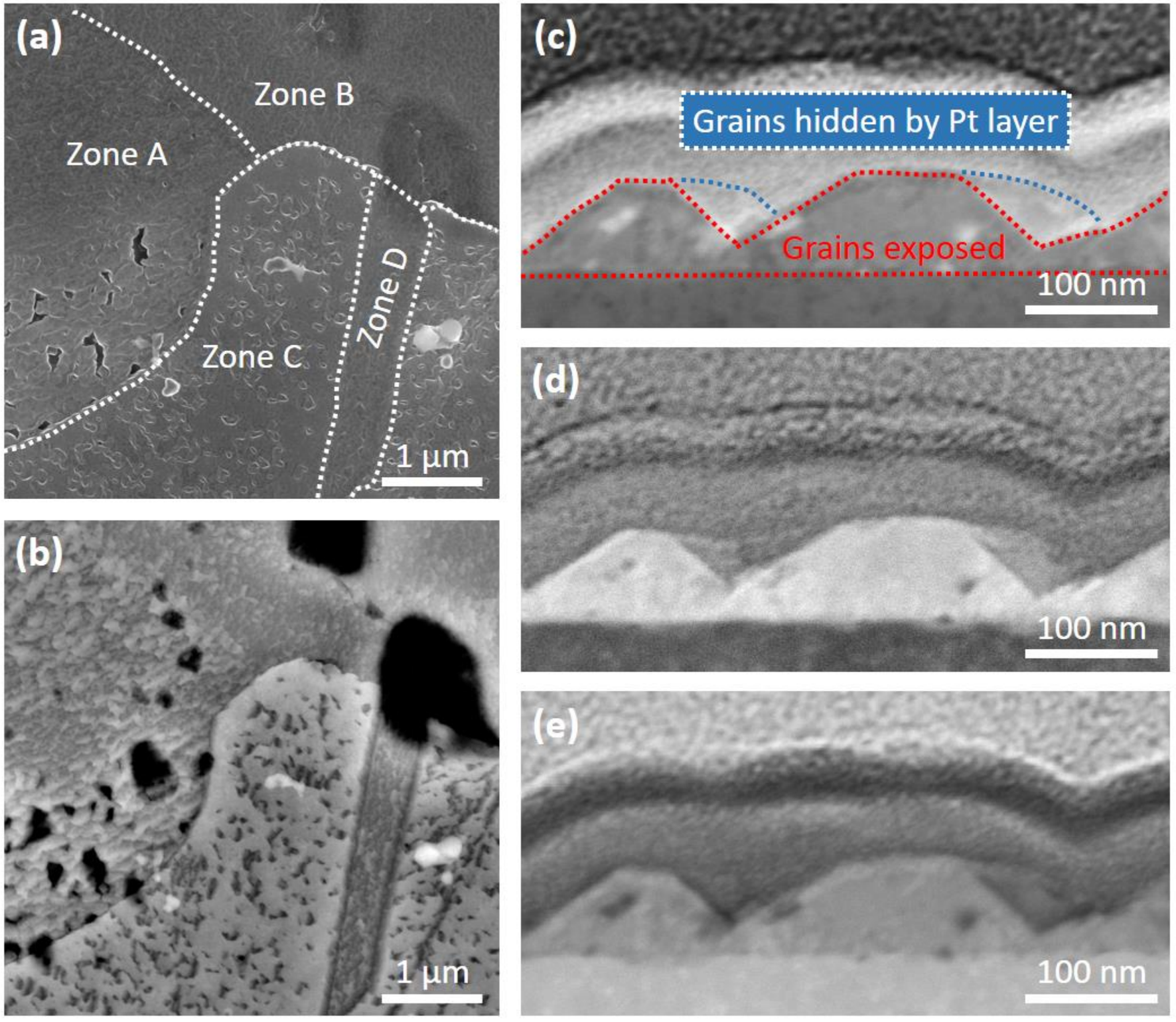
(a)
Zone A
Zone B
Zone C
Zone D
1 µm
(b)
1 µm
(c)
Grains hidden by Pt layer
Grains exposed
100 nm
(d)
100 nm
(e)
100 nm

Figure 6

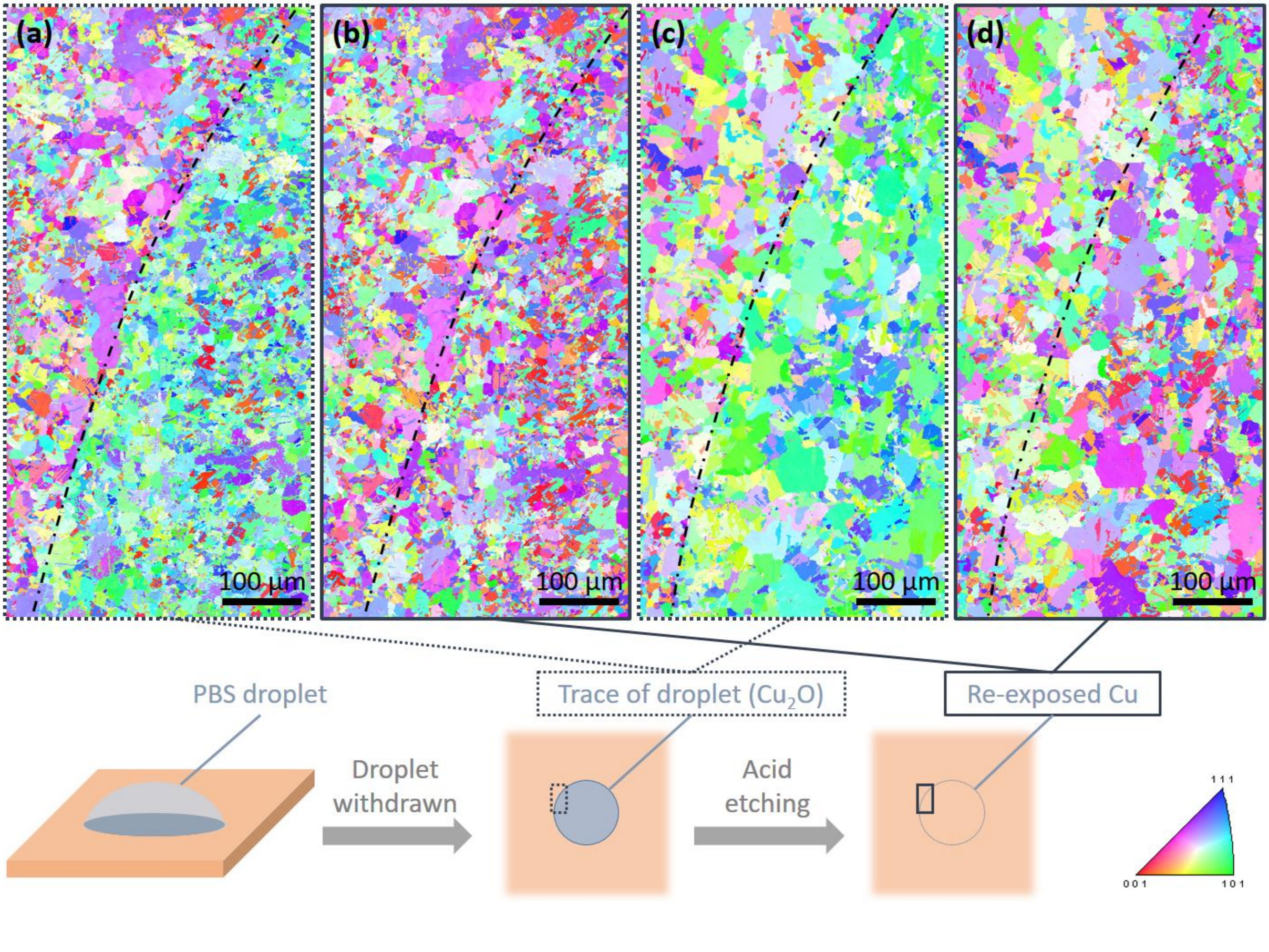
(a)
(b)
(c)
(d)
100 µm
100 µm
100 µm
100 µm
PBS droplet
Droplet withdrawn
Trace of droplet (Cu_2O)
Acid etching
Re-exposed Cu
111
001
101

Figure 7

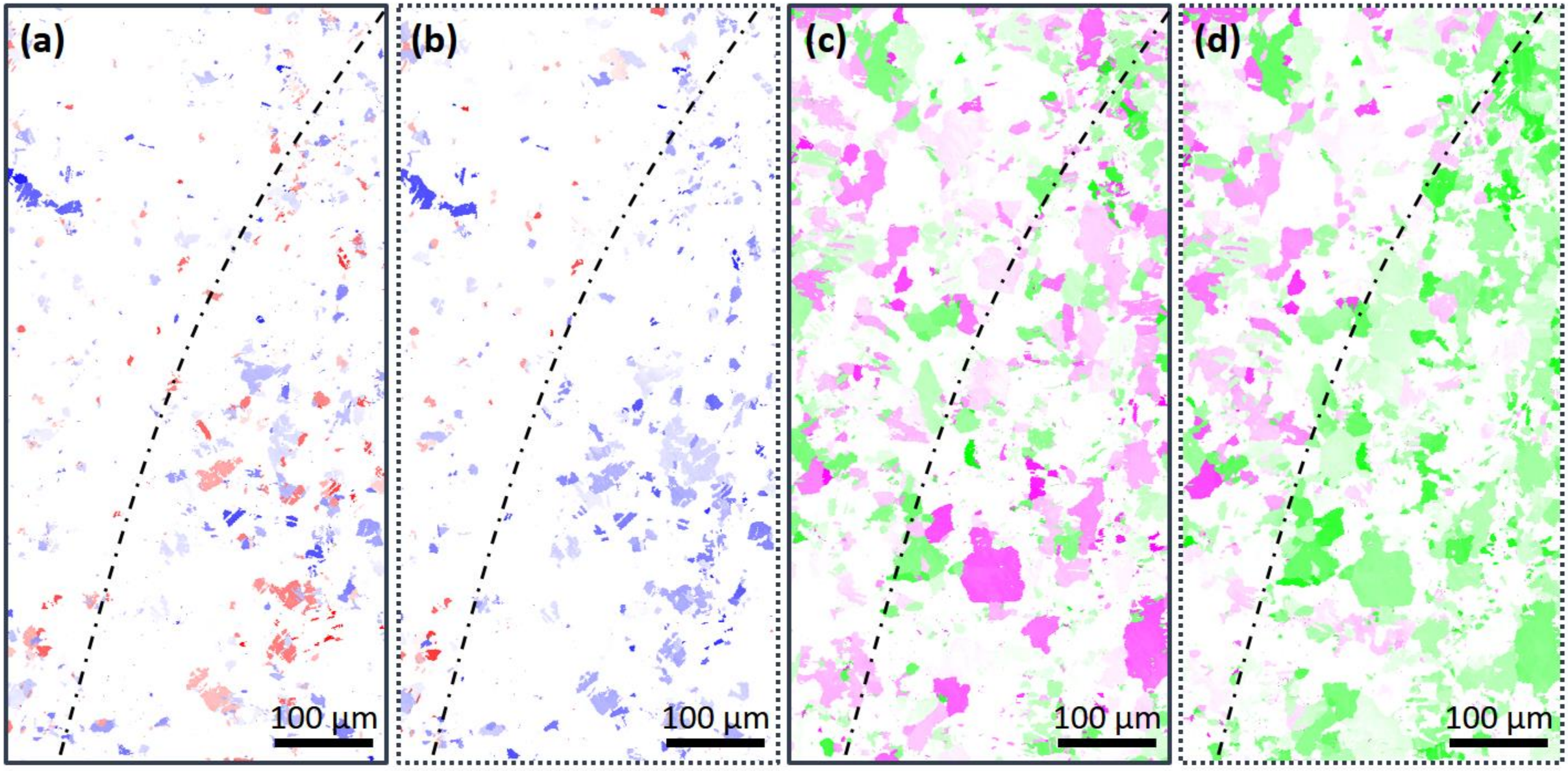
(a)
(b)
(c)
(d)
100 µm
100 µm
100 µm
100 µm

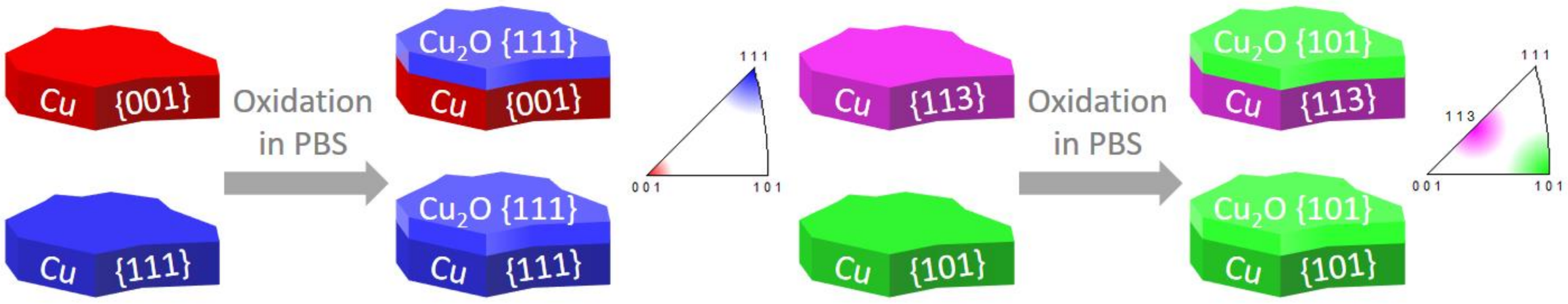
Cu {001}
Cu {111}
Oxidation in PBS
Cu2O {111}
Cu {001}
Cu2O {111}
Cu {111}
111
001
101
Cu {113}
Cu {101}
Oxidation in PBS
Cu2O {101}
Cu {113}
Cu2O {101}
Cu {101}
111
113
001
101

Figure 8

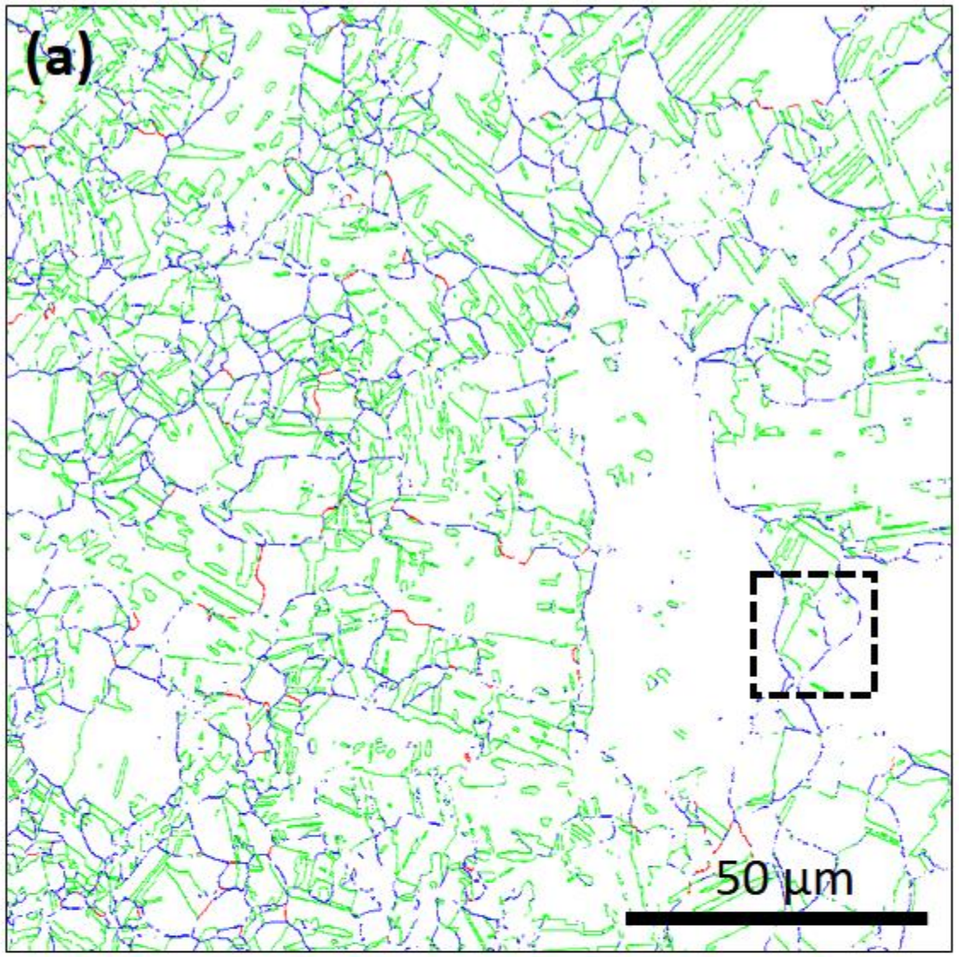
(a)
50 μm

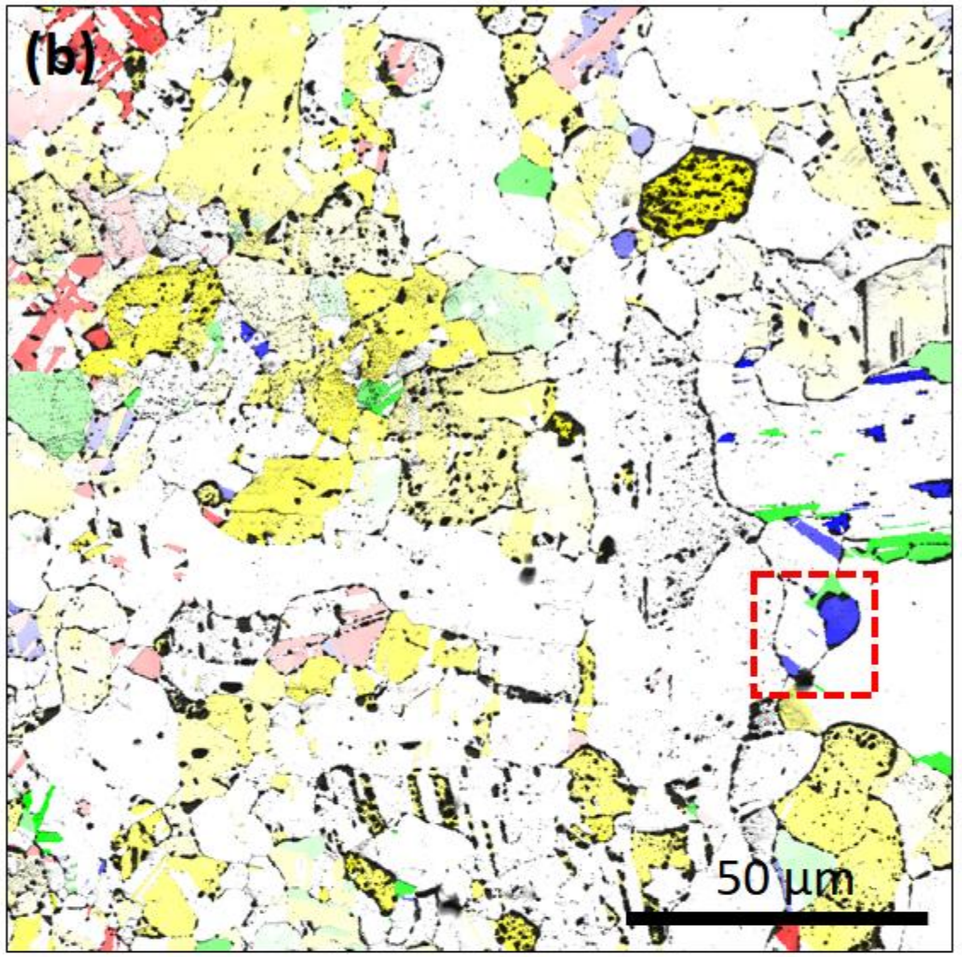
(b)
50 μm

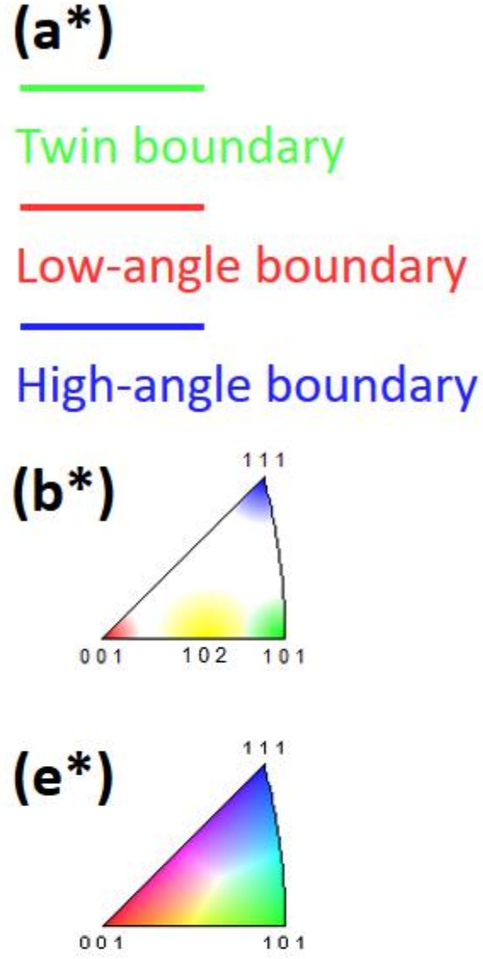
(a*)
Twin boundary
Low-angle boundary
High-angle boundary
(b*)
111
001
102
101
(e*)
111
001
101

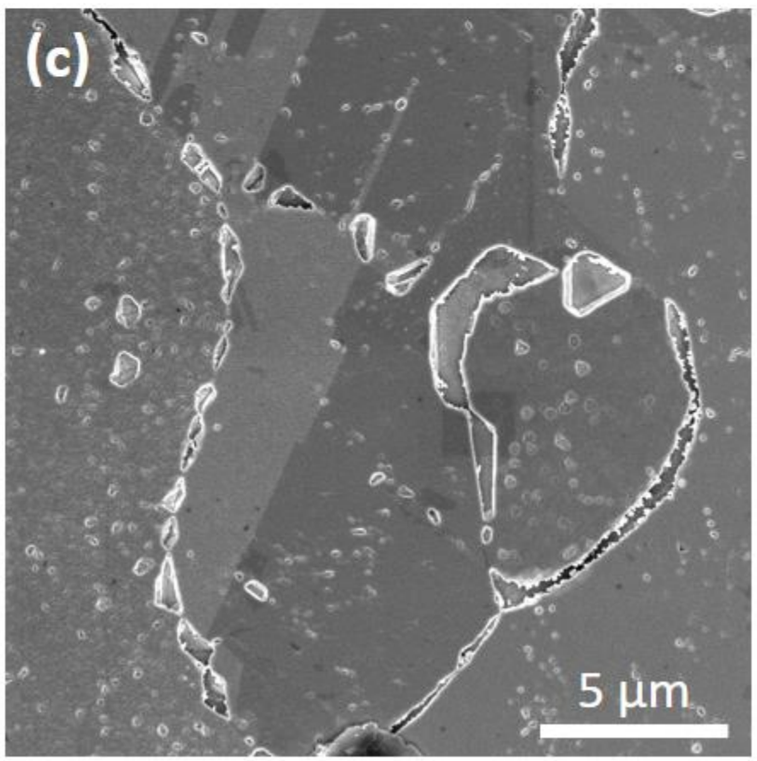
(c)
5 μm

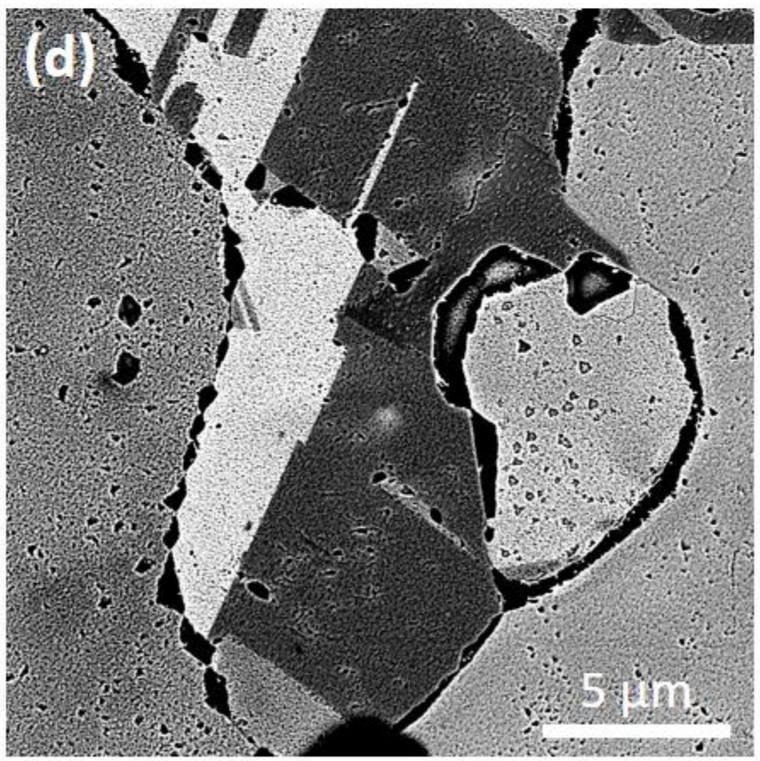
(d)
5 μm

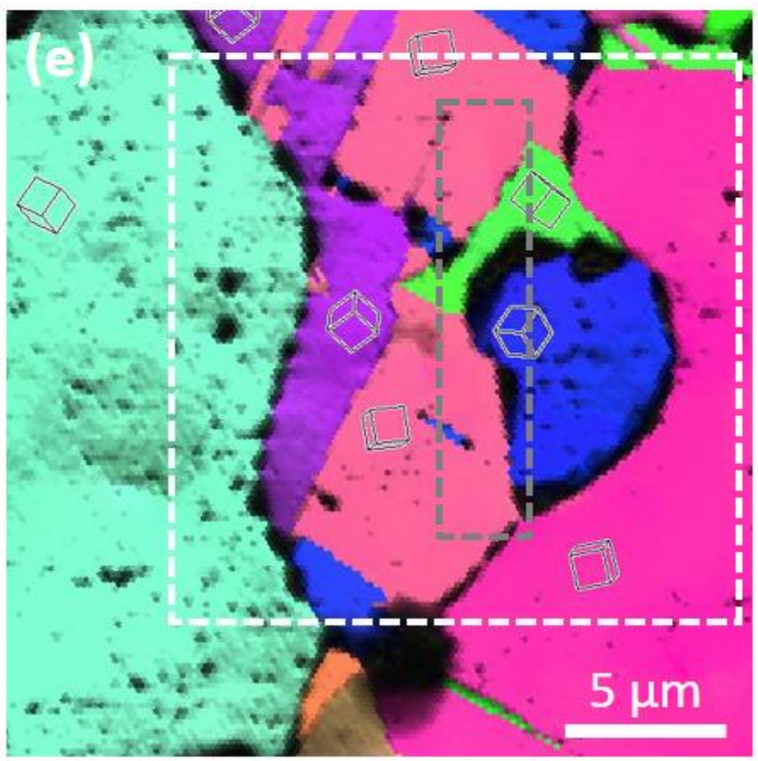
(e)
5 μm

Figure 9

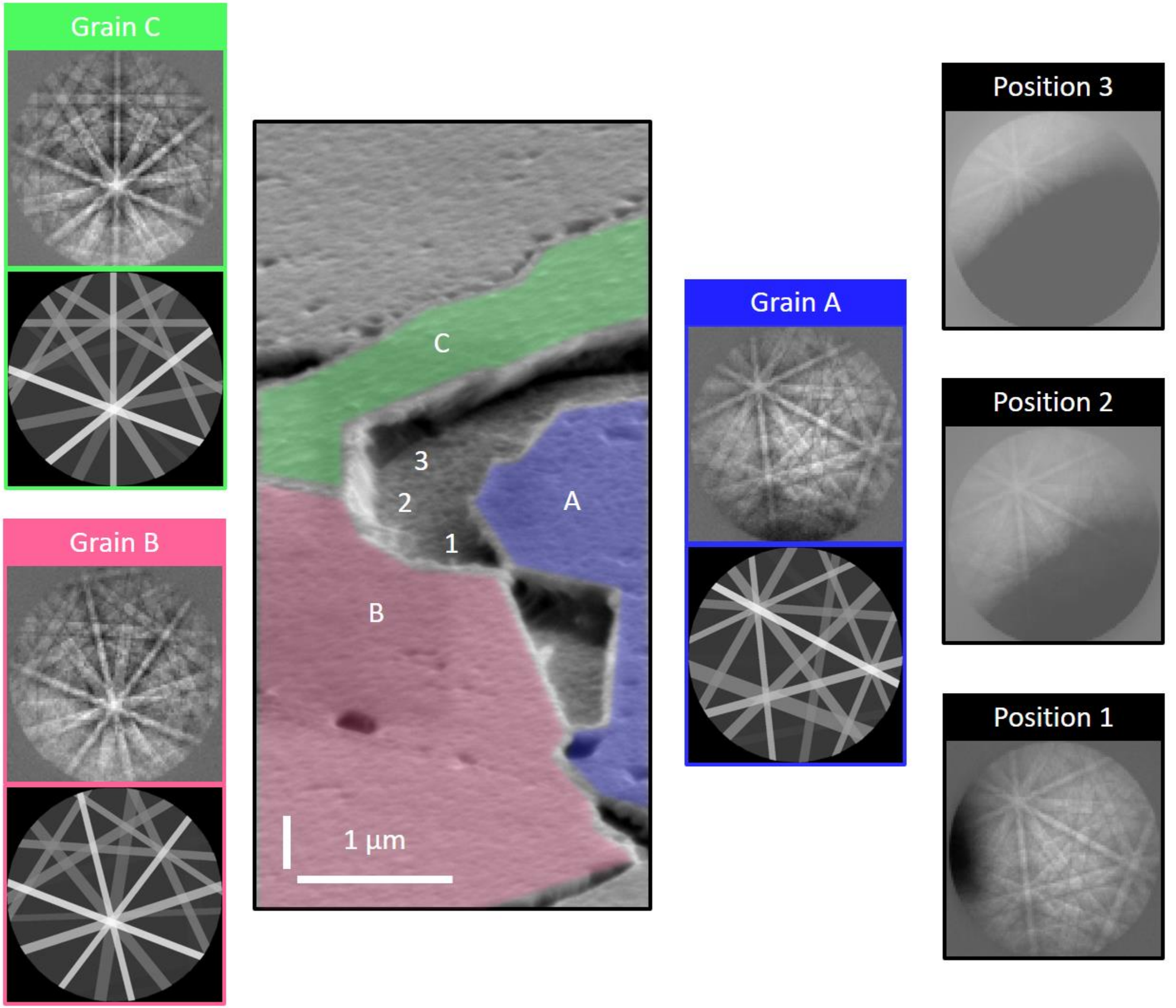
Grain C
Grain B
C
3
2
A
1
B
1 µm
Grain A
Position 3
Position 2
Position 1

Figure 10

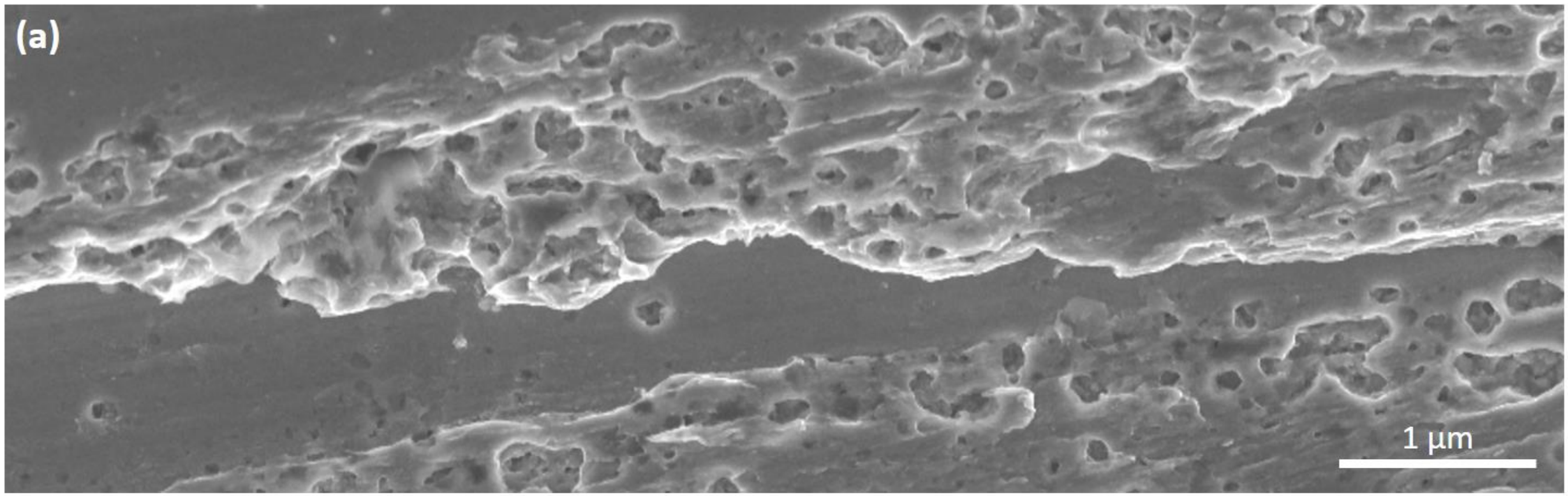
(a)
1 µm
(b)
25 µm
(c)
25 µm
(d)
6h
3h
1h
Cu2O (111)
Intensity (counts)
2 Theta (°)
0
20
40
60
80
100
120
140
160
180
200
34
35
36
37
38

Figure 11

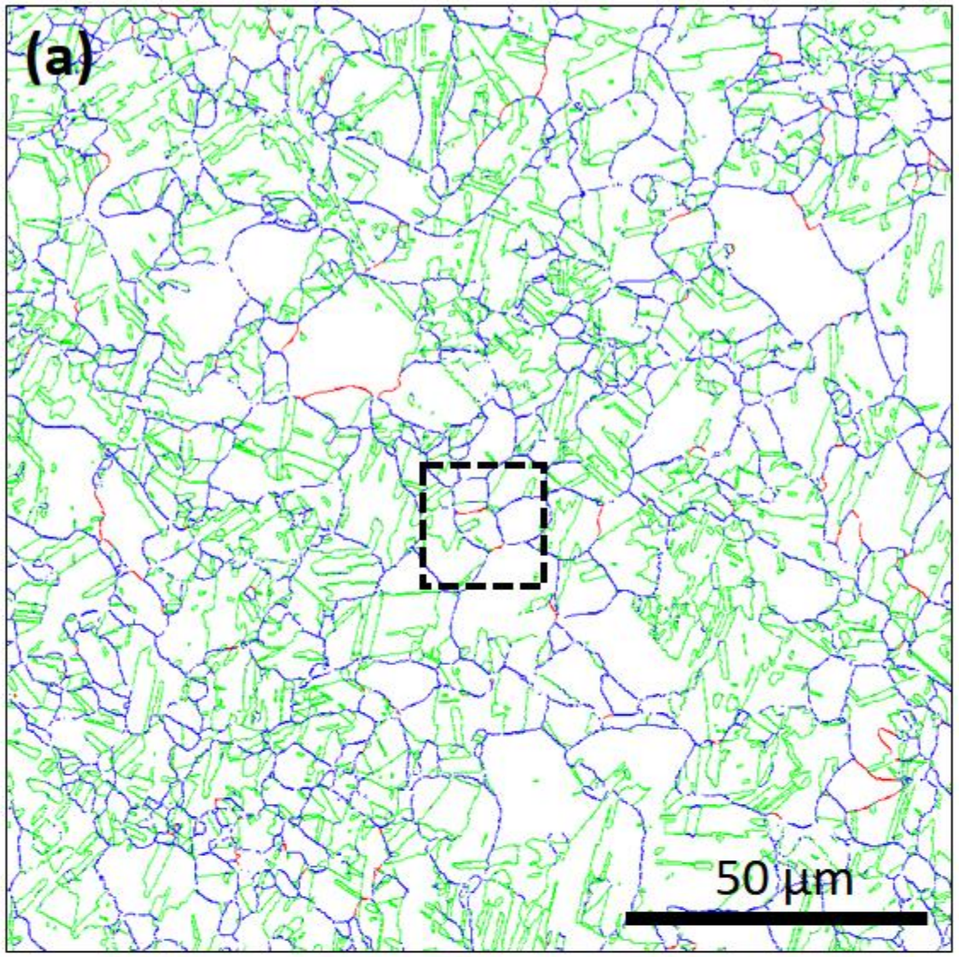
(a)
50 µm

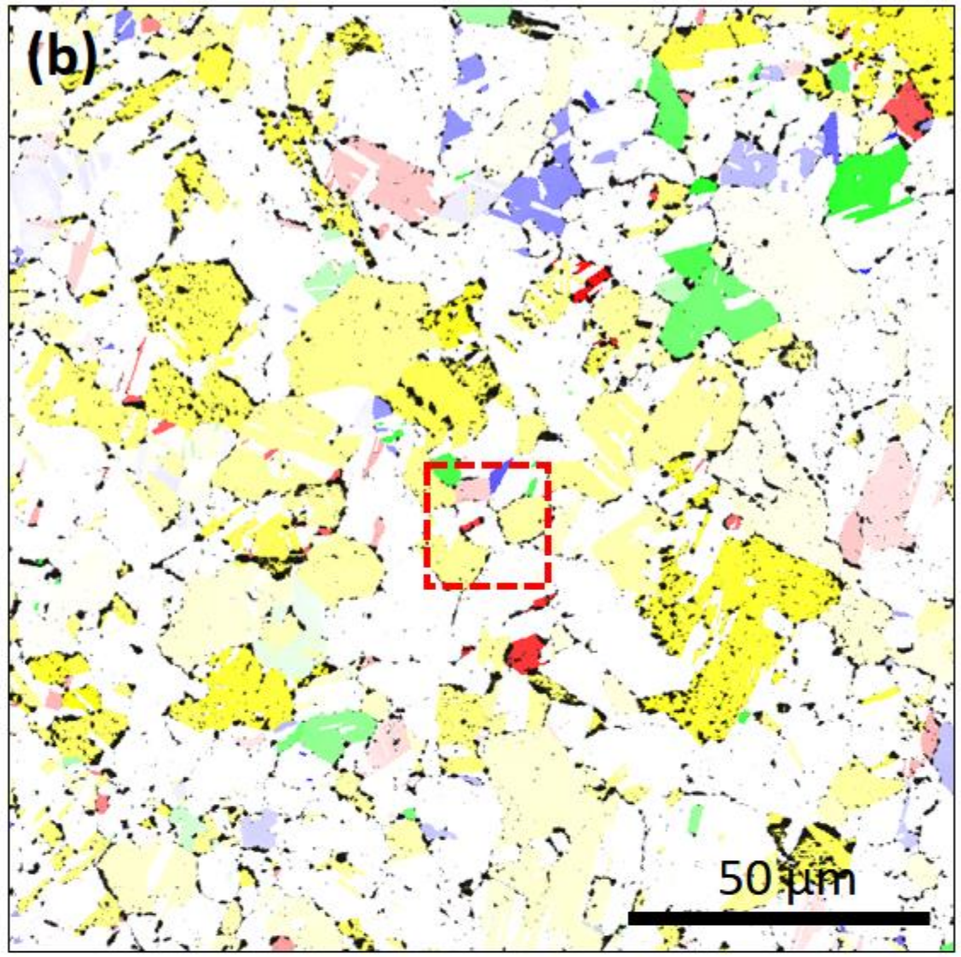
(b)
50 µm

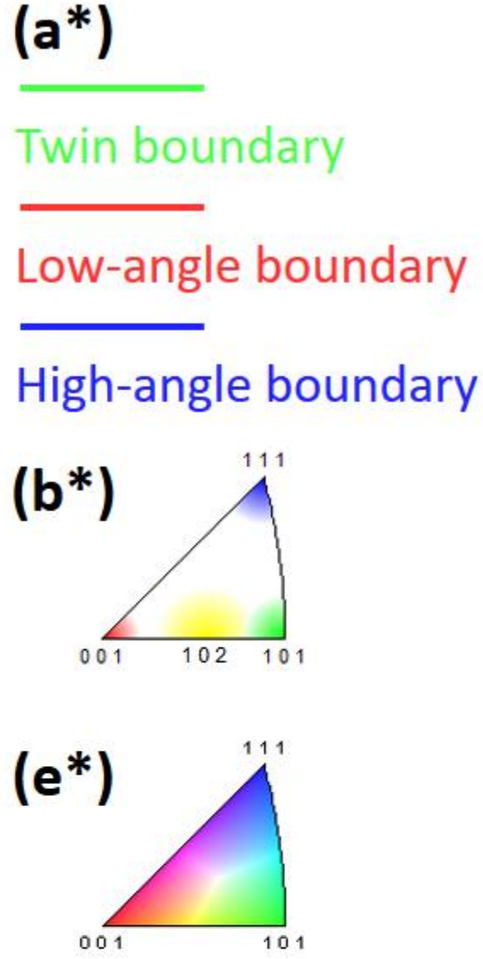
(a*)
Twin boundary
Low-angle boundary
High-angle boundary
(b*)
111
001
102
101
(e*)
111
001
101

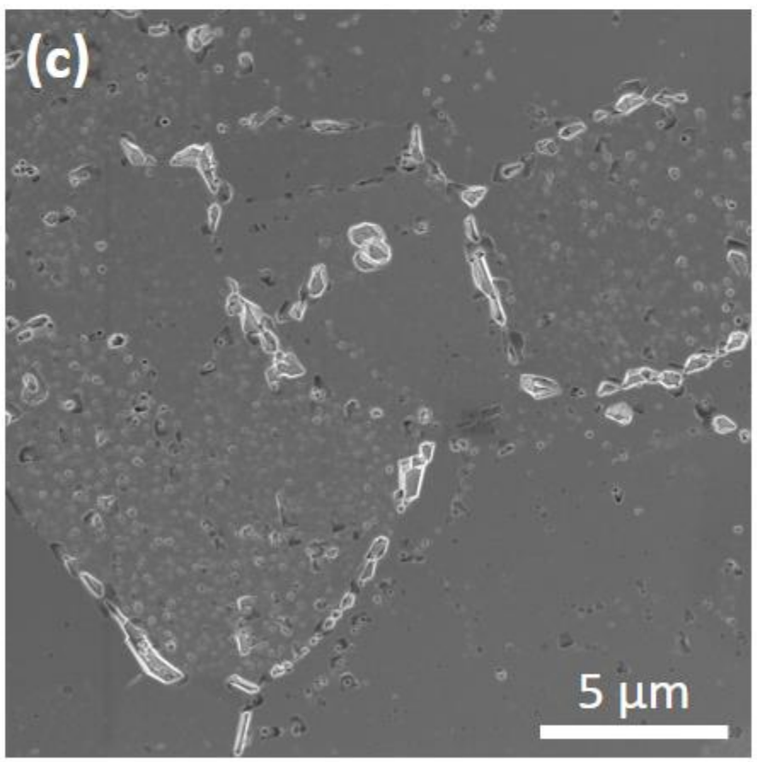
(c)
5 µm

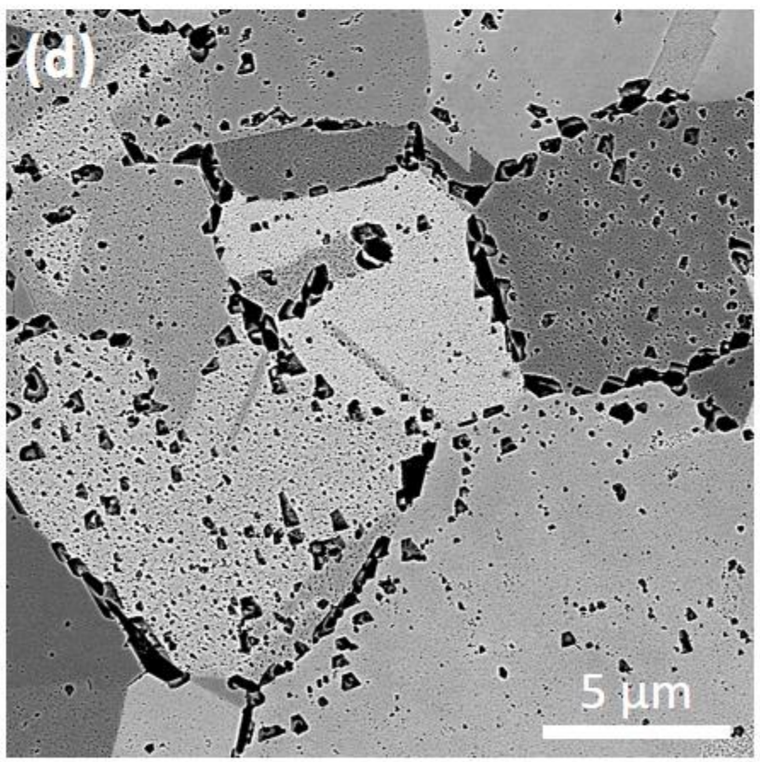
(d)
5 µm

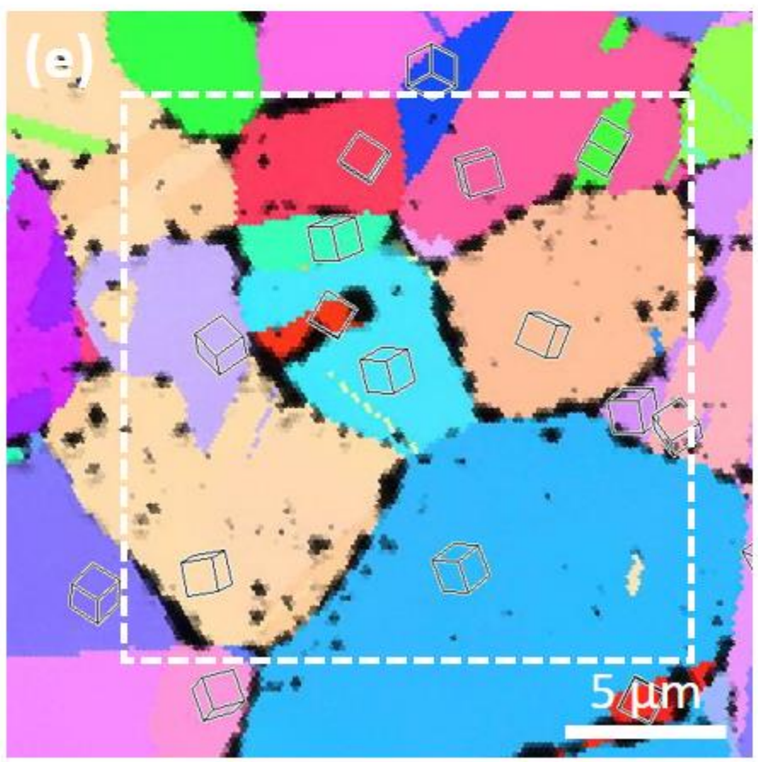
(e)
5 µm

Figure 12

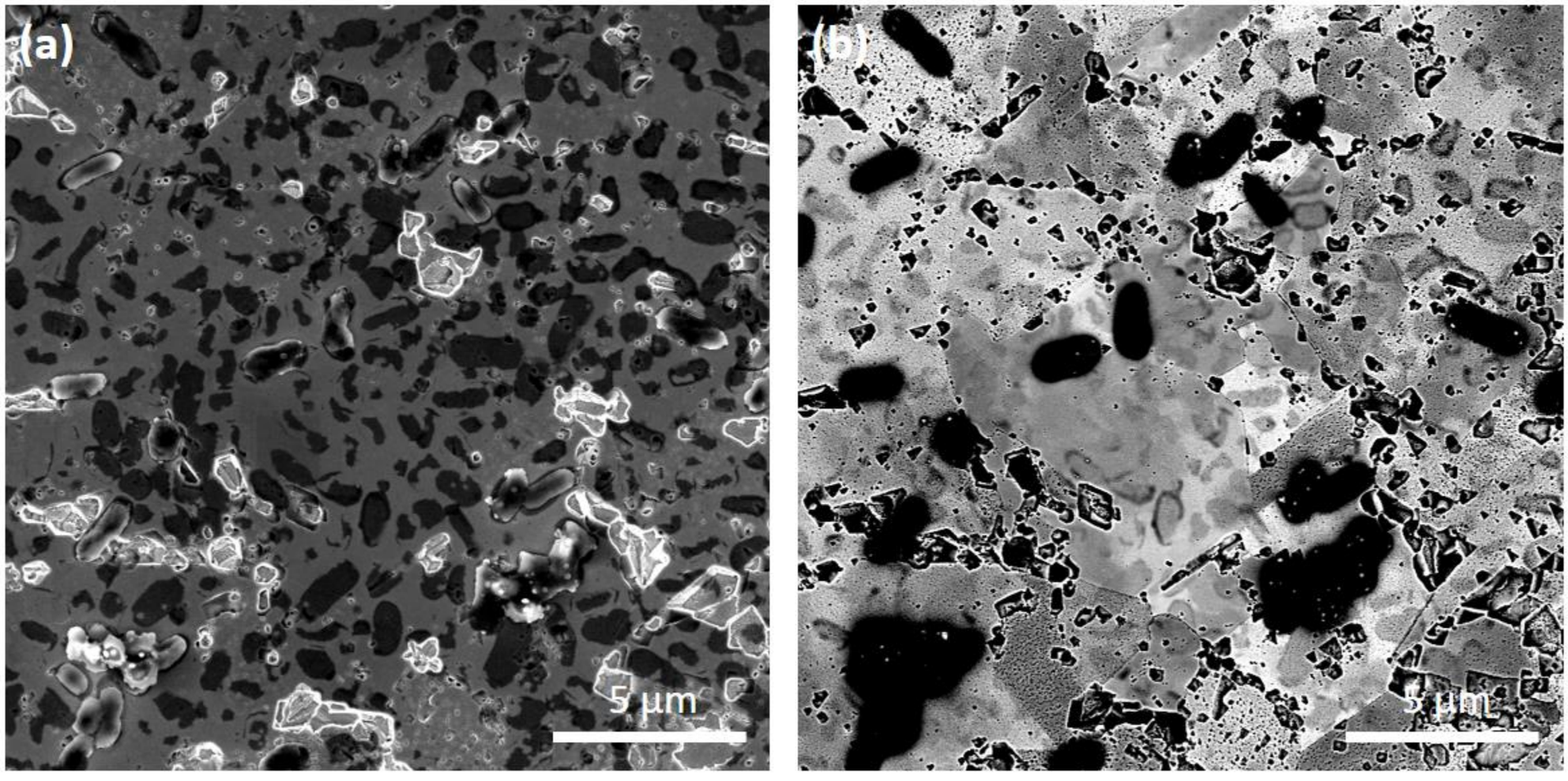

Droplet exposure corrosion test

Copper

PBS

E. coli PBS

Cu_2O

Epitaxial oxide growth

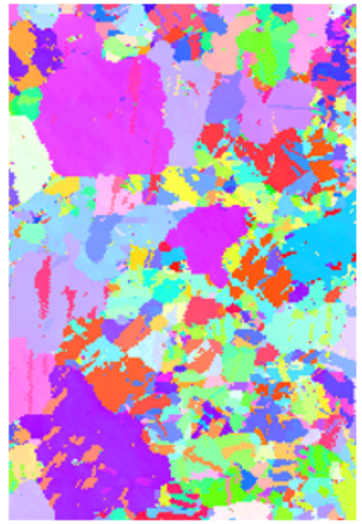

Copper beneath

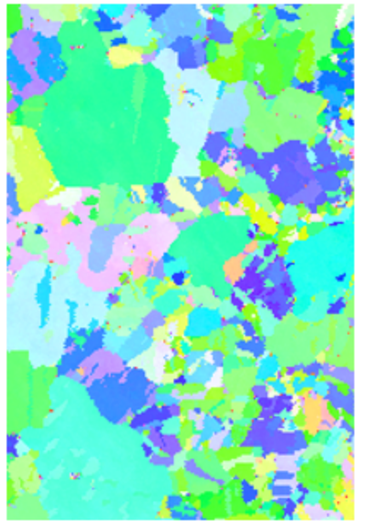

Cu_2O on top

Localised corrosion attacks

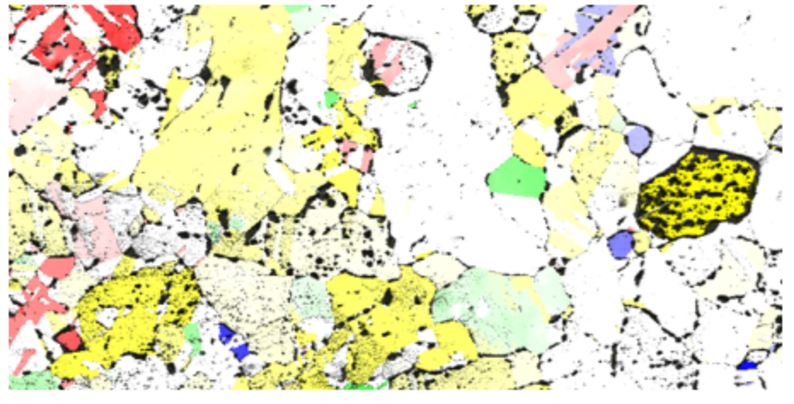

- Intergranular attack
- Crystallographic etching
- …

* *E. coli* did NOT introduce corrosion sites